THESIS FOR THE DEGREE OF LICENTIATE OF ENGINEERING

Effects of Gamma Radiation on Water Chemistry, Polymers and Fe-, Ni- and Zr-Based Alloys

Luca Gagliani

Department of Chemistry and Chemical Engineering

CHALMERS UNIVERSITY OF TECHNOLOGY

Gothenburg, Sweden 2025

Effects of Gamma Radiation on Water Chemistry, Polymers and Fe-, Ni- and Zr-Based Alloys

Luca Gagliani

Technical Report No: 2025:04

Department of Chemistry and Chemical Engineering

Chalmers University of Technology

SE-412 96 Gothenburg

Sweden

Telephone: +046 (0)31-772 1000

Cover:

Left: H_2O_2 concentration, in mM, of γ-irradiated water solution containing ground alloy samples. The samples identified as "H_2O" refer to the vials containing only water; no alloy coupons were submerged in the solution. The received dose at the time of the sampling was 2.2 MGy.
Right: H_2O_2 concentration, expressed in % concerning the original content of 0.15 mM, for solutions containing ground alloy samples. The samples have spent 28 days submersed in the solution before the concentration was measured.

Printed by Chalmers Digitaltryck

Gothenburg, Sweden 2025

Effects of Gamma Radiation on Water Chemistry, Polymers and Fe-, Ni- and Zr-Based alloys

Luca GAGLIANI
Nuclear Chemistry
Department of Chemistry and Chemical Engineering
Chalmers University of Technology

Abstract

Due to the harsh conditions in a nuclear reactor, surface reactions such as metal corrosion, oxide deposition, and oxide release/dissolution are processes that may have a significant impact on the performance of and the occupational safety around nuclear facilities. To maximise the efficiency of the nuclear power plant and minimise the risks, a deep understanding of the mechanisms behind these phenomena is needed, as well as the possibility to test materials on a lab scale. The aim of the project, of which this thesis is a part, is to identify situations where a simplified approach can be sufficient to mimic the surface processes taking place in a nuclear reactor and situations where this is not sufficient.

The goal is pursued through the development and validation of reliable investigative methods and the exploration of oxidation (through SEM, EIS, and XPS), elemental dissolution (ICP-MS) and radiation chemistry (monitoring H_2O_2 concentration) under gamma irradiation.

The results indicate that polysiloxane rubber septa can significantly reduce the radiolytically-produced H_2O_2 by up to 90% compared to polytetrafluoroethylene (PTFE) and aluminium septa, The suppression of H_2O_2 was observed exclusively during irradiation and appears to be related to the availability of oxygen, possibly indicating the consumption of O_2 by radicals in the polymer matrix formed by the radiation, which in turn suppress H_2O_2 formation as O_2 is a precursor for hydrogen peroxide.

As for the investigated alloys, namely AISI 441, Inconel 718, Inconel X750 and Zircalloy-2 low alloy, collected data highlight that different alloy formulations cause different H_2O_2 steady-state in the system (i.e., glass vials containing the metallic coupon and water) and how this phenomenon is triggered by gamma radiations. Moreover, no detectable traces of oxide growth have been detected on the samples, ruling out surface oxidation as the root cause for H_2O_2 consumption. On the other hand, it seems to be possible to correlate the electrochemical response of the alloys under irradiation with their effect on the hydrogen peroxide steady-state concentration achieved during prolonged irradiation (up to 2.2MGy).

Keywords: Gamma irradiation, Polymer degradation, Hydrogen peroxide, Electrochemistry.

List of Publications and Manuscripts

This thesis is based on the following paper:

Paper I (Submitted, under review)

Gagliani Luca, Jonsson Mats, Ekberg Christian, “How Septum Materials Affect H_2O_2 Accumulation under Gamma-Irradiation of Water in Sealed Vials: A Comparative Study on Polysiloxane Rubber, PTFE, and Aluminum”, Radiation Physics and Chemistry, 2025.

Contributions: Conceptualization, L.G.; methodology, L.G.; formal analysis, L.G. and M.J.; investigation, L.G.; writing—original draft preparation, L.G.; writing—review and editing, L.G., M.J. and C.E.; visualization, L.G.; supervision, M.J. and C.E.; funding acquisition, M.J. and C.E.

Table of Contents

List of abbreviations

NPP	Nuclear Power Plant
LWR	Light Water Reactor
PWR	Pressurized Water Reactor
BWR	Boiling Water Reactor
RPV	Reactor Pressure Vessel
EIS	Electrochemical Impedance Spectroscopy
SEM	Scanning Electron Microscopy
ICP-MS	Induced Coupled Plasma Mass Spectroscopy
XPS	X-Ray photons Scattering
EC	Electrochemical
WE	Working Electrode
CE	Counter Electrode
HER	Hydrogen Evolution Reaction
CA	Chronoamperometry
LSV	Linear Sweep Voltammetry
OCP	Open Circuit Potential
HWR	Hot Water Reactor
GCR	Gas Cooled Reactor
MOX	Mixed Oxide
FP	Fission Product
LET	Linear Energy Transfer
PWSCC	Pressurized Water Stress Corrosion Cracking

1. Introduction

The adverse effects of climate change, including rising temperatures, extreme weather events, and melting ice caps, have accelerated global efforts to de-carbonize energy systems, with carbon dioxide emissions from fossil fuel-based electricity generation remaining a primary contributor to climate change[1]. Simultaneously, electricity consumption continues to rise globally due to economic development, digitalization, and the electrification of various sectors, particularly transportation. The International Energy Agency projects that electricity demand will increase by over 50% worldwide by 2050[2]. Renewable energy sources, such as wind and solar, play a crucial role in the clean energy transition but face challenges related to intermittency and storage.

To achieve net-zero emissions by mid-century, a substantial reduction in reliance on coal, oil, and natural gas for electricity generation is required. Nuclear power, with its negligible carbon footprint compared to fossil fuels, stands as a key technology to support this transition by complementing renewables by ensuring a continuous and stable electricity supply[3]. Sweden, with its fleet of six operational light water nuclear reactors, spread over three sites and accounting for 29% of all the electricity production in 2024[4], will see a sharp increase in electricity demand, from the current 140 TWh to a projected 250 TWh in 2035, of which 88 TWh will be needed by the industry alone[5]. While the construction or planning of new nuclear reactors in Sweden[6] and elsewhere[7] are at the highest levels in the last thirty years, the operating nuclear power plants are undergoing life extension evaluation[8]. In Sweden, nuclear power plant owners are also aiming for an extension of the operational lifetime from 60 to 80 years[9], [10].

Operating a nuclear power plant safely and efficiently for decades requires extraordinary engineering precision, rigorous safety protocols, and continuous monitoring. Parts are inspected and replaced at time intervals, eventually requiring the reactor shutdown with subsequent outages. During normal operation of a NPP, the materials are exposed to extreme conditions such as temperatures up to 350˚C for the parts in contact with the coolant (fuel and cladding capable of reaching even higher temperatures), pressure up to 160 atm and continuous irradiation with mainly neutrons and γ radiation. Moreover, corrosive species are formed by the interaction of radiation with the coolant (i.e., radiolytic products). Materials, mostly zirconium-based, nickel-based and chromia-forming alloys, may therefore be subjected to abnormal oxide growth or dissolution, corrosion and re-deposition. Therefore, a need to comprehend the mechanisms behind these phenomena at the solid/liquid interface and how to prevent, limit or act in time before they appear or have a worse effect on the system.

This work as a whole aims at investigating whether it is possible to reproduce, on a laboratory scale and without the use of radiation, the same conditions and effects on certain alloys as those experienced in an actual reactor. This approach would simplify the testing procedure while drastically reducing both time and costs. Given the complexity of the task and the numerous variables involved, and considering that in a nuclear power plant (NPP), material surfaces are exposed rather than existing as powders or slurries, the decision was made to test them under gamma-irradiation and in the form of planar surfaces, such as foils and coupons.

Furthermore, extensive investigations are required to establish a solid foundation for consistent, reliable, and reproducible results. Materials, methods, and equipment employed in the investigations are therefore systematically examined, aiming to develop a reliable experimental procedure that supports the project's objectives. This is crucial because radiation affects not only the samples (intended as both the liquid and solid phase objects of irradiation) but also the containers, making it essential to distinguish between their respective contributions.

Additionally, as no prior studies have been conducted on the radiolysis vs H_2O_2 effect on surfaces, this project represents the first such effort undertaken by our research group, offering insights into how different materials are influenced by gamma radiation and, in turn, how they impact the chemistry of water radiolysis.

2. Background

2.1. Light Water Reactor (LWR) Systems

Light Water Reactors (LWRs) are the most diffused type of nuclear reactor operated for energy production worldwide. According to the International Atomic Energy Agency (IAEA) at the time of the writing of this thesis, out of a total of 416 operational nuclear reactors in the world, 360 are LWRs. Of this total, 306 are Pressurized Water Reactors (PWRs) and 43 are Boiling Water Reactors (BWRs)[11]. Sweden is currently operating a total of 6 reactors, of which only two are PWR at the site of Ringhals Nuclear Power Plant (NPP), while the remaining four at Forsmark and Oskarshamn are BWR[12], [13], [14]. With respect to other kinds of nuclear reactors, such as Heavy Water Reactors (HWRs) and Gas-Cooled Reactors (GCRs), ordinary water (H_2O) is exploited as a coolant and a neutron moderator at the same time. With their relative simplicity, fuel availability and coolant chemistry, LWRs gained large popularity and diffusion, with the first ever built LWR for civilian energy production dating back to 1957, when Westinghouse's PWR at Shippingport 1 plant became operational. The first operational BWR reactor was General Electric's Dresden-1, in 1960.

LWRs operate on the working principle of nuclear fission, where a fissile solid fuel in the form of pellets (generally uranium oxide, UO_2 or mixed-oxide fuel, MOX) is loaded in zirconium alloy rods spaced by metallic spacers and surrounded by coolant, i.e., water. Only a relatively small fraction of the fuel is fissile (i.e, can split into two smaller elements upon being hit by a thermal neutron), with the majority being fissionable (i.e., can only be split by fast neutrons or absorb a neutron and convert into a fissile one such as U^{238} becoming Pu^{239}). Upon thermal neutron collision, the fissile nuclide can split into two (or more) fragments, called fission products (FPs), releasing an average of 2 to 3 neutrons and energy in the form of heat, as in the example reaction given in **Equation 1**.

Equation 1: $$n_0^1 + U_{92}^{235} \rightarrow Te_{52}^{132} + Zr_{40}^{101} + 3n_0^1 + heat$$

The water surrounding each fuel rod and interposing between them will hence collect the produced heat and moderate (i.e., slow down) the released neutrons, which will eventually lead to further fission events or breed more fissile fuel from fissionable nuclei. The hot water will then indirectly (e.g., PWRs) or directly (e.g., BWR) activate steam turbines to convert the heat into electricity. In the subchapters below, a brief explanation of the differences between BWR and PWR will follow.

2.1.1. Pressurized Water Reactor (PWR)

In a Pressurized Water Reactor (PWR), the water is never allowed to transition from liquid to steam in the closed primary circuit (i.e., the parts encompassing the reactor core, where heat is generated and harvested by the primary coolant). For this reason, given the temperatures reached by the coolant during reactor operation, which range from 330 to 350 °C, the Reactor Pressure Vessel (RPV, where fission occurs) is designed to operate at pressures of 150-160 atm[15]. A neutron moderator, boron, is diluted into the coolant in the form of boric acid (H_3BO_3) and control rods are operated from the bottom of the RPV. The hot primary coolant is then circulated to the steam generators, where the heat is transferred through heat exchangers to a secondary coolant (i.e., water) allowed to evaporate and activate the turbines for electricity production. As visible in **Figure 1**, the primary coolant is then circulated back to the RPV. This design allows for a radioactivity-free secondary circuit, confining all the active substances in the primary circuit.

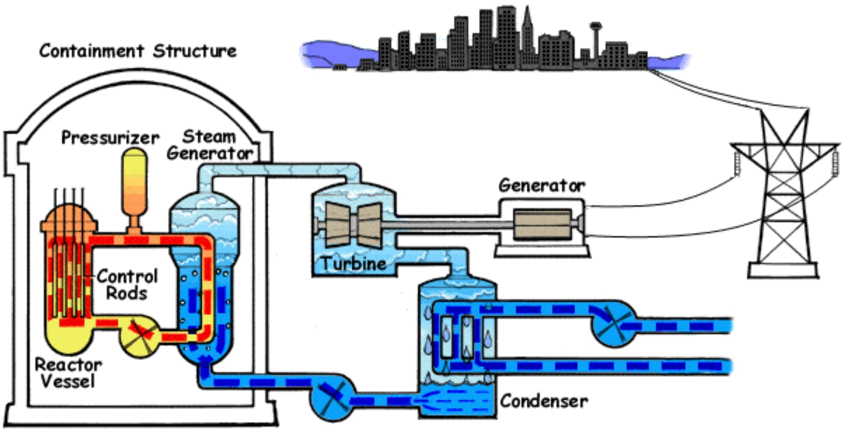

Figure 1: Schematic representation of a PWR reactor and its main constituents, from the U.S. NRC website[16]

2.1.2. Boiling Water Reactor (BWR)

In a Boiling Water Reactor (BWR), the primary coolant generally reaches temperatures in the range of 270-290 °C while kept at lower pressures with respect to the PWR. Said pressures are in the order of 70 bar, allowing the water to become steam[15]. In the RPV of BWR systems, the main cooling is therefore actuated by a mix of water and steam. Short-term moderation of the fission reactions is also achieved by water evaporation. The larger the amount of heat generated, the larger the portion of water converted into steam, and hence, the smaller the moderating effect generated by the water. Old BWR designs, somehow similar to PWR, were characterized by steam turbines operated by a secondary closed system through heat exchangers. Such a design has been completely dismissed. More recent BWRs operate the turbines directly with the steam generated in the RPV, after accurate dehumidification and filtering. The steam is then condensed, purified, pre-heated and pumped back to the RPV. The risk of radioactive contamination/spill can be judged as sensibly greater than for PWRs since the major complexity is due to the operation of turbines with steam directly spilled from the vessel, as schematized in **Figure 2**.

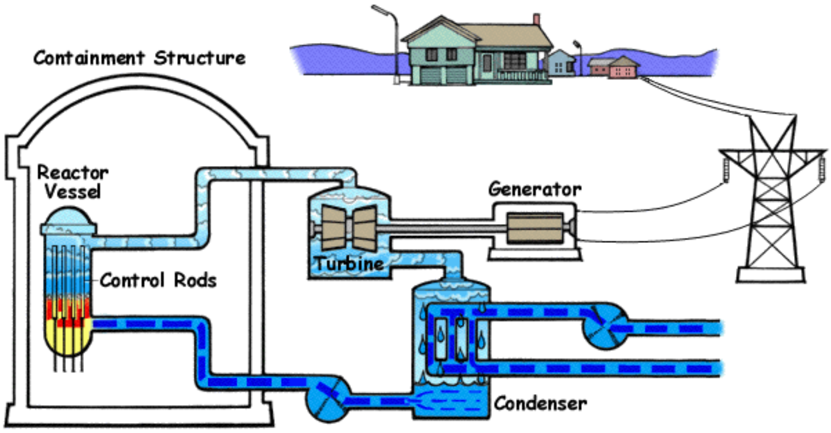

Figure 2: Schematic representation of a BWR reactor and its main constituents, from the U.S. NRC website[16].

The exception for the dual use of water as both coolant and moderator in BWRs is represented by the RBMK reactor units. Such a design was ideated in Russia, and several NPPs were built in the Soviet Union exclusively. The main design difference of RBMKs is that the moderation is provided by graphite bars and only the cooling of the core is done by water, which circulates in separate cooling channels.

2.2. Radiolysis of Water and Chemistry of Water in LWRs

Similarly to electrolysis, where water is decomposed into molecular oxygen (O_2) and molecular hydrogen (H_2) respectively at the anode and cathode of a polarized circuit, radiolysis consists in the decomposition of water molecules due to the interaction with ionising radiation. Ionising radiation, such as electrons, neutrons, X-rays, gamma- and alpha-radiation, can excite and ionise molecules along its path. Water radiolysis is always present in water-cooled reactors, taking place in the coolant and at the interface between coolant and solids (e.g., the fuel cladding). The ionising radiations responsible for water radiolysis in LWRs are mostly gamma and neutrons. Given the range of alpha and beta particles, they can contribute only in the event of a direct fuel-coolant interaction (hence, a cladding failure or incident) or activated particle-coolant interaction. As presented in **Figure 3**, the radiolytic event can be visualised in three stages, differentiated by the time scale.

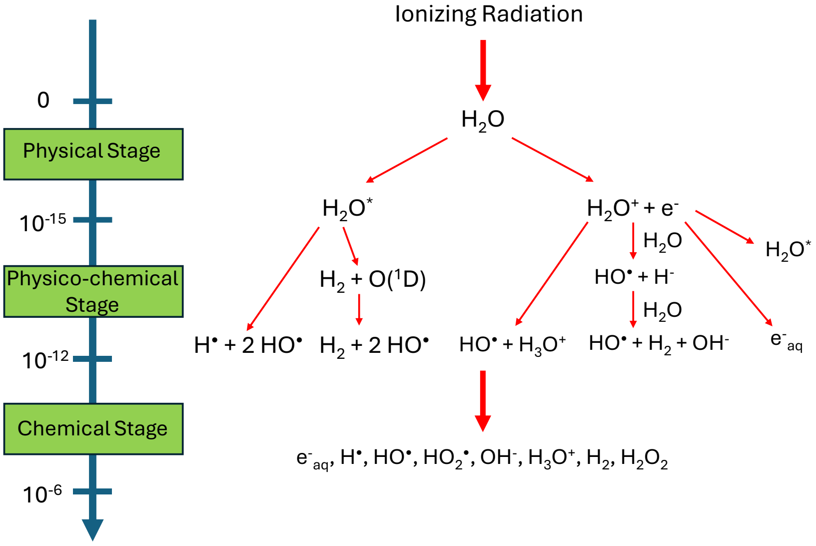

Figure 3: Main reactions involved in the radiolysis of water, Inspied by "Water Radiolysis: Influence of Oxide Surfaces on H2 Production under Ionizing Radiation", S. Le Caër, 2011[17].

During the first stage (i.e., physical stage, 0-10^{-15}s) excited (H_2O^*) and ionized (H_2O^+) water molecules originate from the interaction with the ionizing radiation. In the second stage (i.e., physicochemical stage, 10^{-15}-10^{-12}s) different processes such as ion-molecule reaction, dissociative relaxation, ionization of excited states, solvation of electrons and hole diffusion, (just to name a few) take place. The third stage (i.e., chemical stage, 10^{-12}-10^{-6}s) is characterized by the species reacting with each other within the tracks and/or with the surrounding molecules so far unaffected by the irradiation. Thus, the products in the tracks diffuse to the surroundings leading to further chemical reactions. For low-LET radiation, (i.e., γ-radiation) recombination's contribution is therefore irrelevant after 10^{-6}s.

The production yields for water radiolysis have been largely investigated and depend on several factors, such as the time from the initial radiation-molecule interaction, the solution's pH and the presence and kind of solutes. Being most of the radiolysis products very reactive/unstable (e.g., radicals, solvated electrons), they will rapidly disappear. The primary oxidative radiolysis products in gamma-irradiated water are then hydrogen peroxide (H_2O_2), the hydroxyl radical (HO•) and to some extent also the hydroperoxyl radical (HOO•), even if in negligible quantities. Molecular oxygen (O_2) is subsequently formed as a secondary oxidative radiolysis product.

Continuous gamma irradiation is known to produce low, stable, concentrations of dihydrogen and hydrogen peroxide due to reactions where their radiolysis production rate is matched by their consumption, caused by the interaction with H• and HO• radicals, as firstly described by Allen [18] and shown in **Equation 2** and **Equation 3**. Clearly, this is a simplified system, but for the practical purposes in this work, it will suffice.

Equation 2: $HO\cdot + H_2 \rightarrow H_2O + H\cdot$

Equation 3: $H\cdot + H_2O_2 \rightarrow H_2O + HO$

As a matter of design, BWRs need very pure water to work flawlessly and avoid issues such as the buildup of deposits on the heat exchangers and turbine blades or selective corrosion phenomena. Impurities (in traces) that may be introduced in the feedwater of the reactor are iron, nickel, chromium, chloride and silica, mainly. For such reasons, precautions are taken and ion exchangers are used to entrap contaminants from the condensate. However, only dissolved species can be effectively removed, since suspended solids are generally deposited on the surfaces of the primary system. In order to protect the surfaces of the primary system from the uptake of contaminants and activated products (e.g., Co^{60}) and add some corrosion resistance, zinc and sometimes noble metals are added in the reactor core water is used[15].

On the other hand, PWRs require a more complex balance of additives in the coolant of the primary circuit. In fact, the moderation and control of the core activity is split between the control rods (for the short-term activity changes) and dissolved H_3BO_3 (for the long-term activity changes). While the addition of boric acid is necessary as a neutron moderator, this induces a lowering of the pH of the coolant, possibly causing both selective dissolution of elements from the RPV and the deposition of the same on the fuel rods in substantial amounts, with repercussions on the contamination build-up within the primary circuit. To balance the pH of the primary coolant, alkali agents such as lithium hydroxide (LiOH) and potassium hydroxide (KOH) are used. Over the years, evidence has been collected that operating PWRs at slightly basic pH values (i.e., pH 7.4) is beneficial for corrosion protection[15]. However, high pH values are again detrimental for the fuel assembly corrosion and primary water stress corrosion cracking (PWSCC), which seem to be accelerated by Li. Since Li^7 is nevertheless produced in the primary coolant by neutron capture and subsequent alpha particle emission by B^{10}, it is preferred over potassium.

2.3. LWRs Criticalities Related to Radiolysis of Water

During LWR operation, primary and therefore secondary products of water radiolysis will accumulate in the irradiated coolant. As listed in 2.2., the longer-living primary products are the OH radical, H_2, H_2O_2 and O_2 as secondary products. Of these, in PWR systems, O_2 is regarded as the most dangerous since able to accelerate Zircaloy corrosion, followed by H_2O_2 (due to its major instability at high temperatures) and H_2. To contain dioxygen buildup, H_2 is injected into the primary coolant[19].

The maximum concentration of O_2 allowed in the primary coolant is usually 0.01 ppm, and a hydrogen-to-oxygen ratio of at least 240 (about 1 mg/kg) is required to maintain such a condition[15]. However, H_2 addition also brings drawbacks, and its concentration cannot exceed 4 mg/kg due to the risks associated with hydrogen uptake in the RPV, especially by the Zircaloy fuel cladding. Hydrogen uptake is known to induce alloy embrittlement and hence an increased risk of failures in the long term.

Similarly to PWRs, in BWRs dioxygen and dihydrogen are unwelcome products of water radiolysis. However, the different designs and cooling principles (i.e., liquid vs liquid + steam) lead to a different approach. The vigorous boiling of the primary coolant during operation tends to strip the water of the radiolytically produced gases, preventing their recombination and hence extinguishing the formation of secondary products. Due to the partitioning of gases between liquid and steam, the latter contains up to 10^2 more O_2 and H_2, which are therefore transported to the turbines and the condenser. There, they will be recombined into water through a catalytic process. Hydrogen peroxide, which is an oxidant stronger than dioxygen (the Standard Reduction Potential vs SHE is +1.78 for H_2O_2 and +1.23 V for O_2[20]), is present in concentrations similar to dioxygen in the reactor, despite the sampling systematically showing lower concentrations due to the catalytic decomposition of the same along the sampling line[21]. However, in addition, dihydrogen is also injected into the coolant of BWRs as a further means to control the level of oxidants of peroxide.

2.4. Effect of γ-Irradiation on Polymers

Since the early 1950s, it has been well-known by the scientific community that polymers undergo large changes in their physical properties when exposed to even relatively small doses of radiation[22], [23], [24], [25]. During irradiation, two main types of alterations take place: cross-linking and degradation. Both phenomena alter the molecular weight of the affected polymers and are propagated by the formation of radicals, driving further reactions. The predominant type of degradation depends on factors such as polymer structure, the spatial arrangement of atoms within the molecule and irradiation conditions. As a rule of thumb, the polymers with a structure $-CH_2-CHR-$ (e.g., polyethylene, polystyrene and polyacrylonitrile) are mostly affected by cross-linking. On the other hand, branched polymers, like polyisobutylene, polymethylmethacrylate (PMMA) and polytetrafluoroethylene (PTFE) typically exhibit degradation due to steric strains. Both types of deterioration affect the mechanical strength of the materials.

During cross-linking, the molecular weight of the polymeric chain increases due to the bonding of multiple polymeric chains, creating a three-dimensional network. Cross-linking reduces the solubility of the polymeric chains and alters melting behaviour. As the cross-linked network grows, polymers reach a "gel point," beyond which they become insoluble. The dose required to achieve gel formation depends on the polymer's initial molecular weight and the number of cross-links formed per 100 eV absorbed. During degradation, the molecular weight is reduced due to the breaking of the polymeric chain. Factors like the polymer's initial molecular weight, the irradiation temperature and oxygen availability are particularly relevant for this type of deterioration. In this Licentiate thesis work two polymers have been investigated in particular: PTFE and polysiloxanes (silicone rubber).

Despite its thermal and chemical stability, PTFE degrades readily under radiation, releasing corrosive gases and forming unsaturated fluorocarbon species. These gases include fluorinated species associated with chain scission, which leads to the formation of unsaturated fluorocarbon structures such as $–CF=CF–$ and $–CF=CF_2$ groups within the remaining polymer. The evolution of these reactive gases is linked to the breakdown of the polymer backbone and contributes to oxidative processes if oxygen is later introduced into the irradiated material.

Polysiloxanes, or silicones, exhibit notable cross-linking upon irradiation, with yields ranging from 2.5 to 4.5 cross-links per 100 eV absorbed. This cross-linking improves the mechanical strength and elasticity of silicone rubbers, which are widely used in radiation-rich environments. Unlike many organic polymers, polysiloxanes do not develop unsaturation or color changes during irradiation, likely due to the stability of their silicon-oxygen backbone.

Gaseous byproducts, including hydrogen, methane, and ethane, are evolved during the process. Additionally, polysiloxanes containing phenyl groups demonstrate enhanced radiation resistance compared to dimethyl-substituted silicones due to the stabilising effect of the aromatic rings.

3. Methods

3.1. The Triiodide (Ghormley) Method

The triiodide method is a widely used analytical technique in radiation chemistry for detecting and quantifying hydrogen peroxide (H_2O_2), a radiolytic product formed during the irradiation of water and aqueous solutions, as presented in Chapter 2.2. This method leverages the reactivity of H_2O_2 with iodide ions (I^-) under acidic conditions to produce triiodide ions (I_3^-), which can be measured spectrophotometrically due to their distinct absorbance peak. The chemical reactions involved in the method are shown in **Equation 4** and **Equation 5**.

Equation 4: $H_2O_2 + 2I^- + 2H^+ \rightleftharpoons I_2 + 2H_2O$

Equation 5: $I_2 + I^- \rightleftharpoons I_3^-$

The triiodide ion (I_3^-), is characterized by a strong yellow-orange colour and by measuring the absorbance at a wavelength of 350 nm, the concentration of H_2O_2 can be accurately determined in accordance with Lambert-Beer’s law for the correlation of the absorbance of a diluted solution with the concentration of the solute, as shown in **Equation 6**.

Equation 6: $A = \mathcal{E} \cdot C \cdot l$

Where A is the absorbance of the sample, $\mathcal{E}$ is the molar absorption coefficient, in $m^{-1}cm^{-1}$ and l is the optical path length.

3.2. Electrochemical Analysis Methods

Electrochemical measurements are performed in an electrochemical cell. In a three-electrodes configuration, the setup is constituted by the following main components:

-Working Electrode (WE)
-Counter Electrode (CE)
-Reference Electrode (RE)
-Electrolyte
-Potentiostat

The sample under study is defined as the working electrode and its potential is constantly measured or controlled with respect to the reference electrode. The reference electrode is usually Ag/AgCl 3M or a saturated calomel electrode (SCE) whose potential remain constant in the working conditions (non-polarizable electrode). The third and last electrode in this kind of circuit is the counter electrode. Usually made of inert material for the electrolyte in use, such as graphite or platinum, have the role to close the circuit, supplying/accepting electrons to/from the working electrode. Reactions happening at the working and counter electrodes involve oxidation and reduction, depending on the potential and the ambient conditions. When the working electrode is polarized in the anodic direction (more positive potential than the electrode's open circuit potential, OCP), oxidation reactions will occur with the release of electrons that will be transported to the counter electrode, where a cathodic reaction takes place. Vice versa, if the working electrode is polarized in the cathodic direction (more negative than its open circuit potential), the electrode can perform reduction reactions while taking electrons from the counter. The amount of electrons involved in these reactions, i.e., an electrical current, can be measured: it represents the speed of the process. To close the circuit and allow the flow of a current, the three electrodes must be immersed in an electrolytic solution, where dissolved ions allow the conduction of electricity through the movement of the ions themselves but not of the electrons. Such ions may just serve as conductors, without taking part in any reaction or being involved in chemical reactions at the electrode sites. For such a reason, the choice of an electrolytic solution must be wisely performed, to prevent, limit or consider the bias that such reactions may have on the performed measurements.

Potential and current can be monitored, recorded and/or imposed through the potentiostat. Such a device can be used in DC (direct current) or AC (alternating current) mode. When operated in DC mode, the electrochemical response of the system is time-resolved, i.e., the potential (linear and cyclic voltammetry or chronopotentiometry) or current (linear and cyclic amperometry, chronoamperometry) is recorded as a function of time, while the other variable (current and potential, respectively) is modified by steps, pulse or sweep. When an AC investigation is performed (e.g., EIS, electrochemical impedance spectroscopy), the electrochemical response of the system is recorded as a function not of time but of frequency, which is the frequency of the perturbation imposed over the applied potential or current.

3.2.1. Open Circuit Potential

The Open Circuit Potential (OCP) is a fundamental electrochemical parameter that provides insight into the equilibrium potential of a working electrode in the absence of any externally applied current. This unperturbed potential reflects the balance of electrochemical reactions occurring at the electrode-electrolyte interface. The OCP is measured by allowing the system to stabilize after immersing the working electrode in the electrolyte and recording the potential over time versus the reference electrode. A stable OCP indicates that the system has reached equilibrium with the solution and the gases dissolved in it. OCP is widely used to assess the corrosion behavior of metals: a more negative OCP usually indicates higher susceptibility to oxidation (hence, corrosion), whereas a more positive OCP may suggest the formation of a protective film (e.g., passivation). Monitoring the OCP over time, the development of oxides, passivation layers or corrosion at the electrode/electrolyte interface can therefore be studied by highlighting a change in the equilibrium state of the material due to the newly formed surface in contact with the solution. Factors such as the composition of the alloy, surface finishing and roughness, and pre-existence of an oxide layer may affect the measurements. Also, the type of electrolyte (i.e., pH, presence of halogens ions, etc..), the temperature and the availability of oxygen may greatly affect the measurements. It is also of paramount importance to allow the system to stabilize for sufficient time before performing the measurements. Depending on the abovementioned factors, the stabilization of the OCP may take from a few minutes up to hours. The selection of the correct time for the stabilization before the beginning of new surface reactions (e.g. corrosion and formation of oxide layers) must be carefully studied.

3.2.2. Linear Voltammetry

Linear Sweep Voltammetry (LSV) is an electrochemical technique used to study redox processes, electrochemical kinetics, and reaction mechanisms at electrode surfaces[26]. In LSV, the potential of the working electrode is linearly swept over time at a fixed scan rate (in mV/s) from an initial value of potential to a final one selected by the user. In the meantime, the current resulting from oxidation or reduction phenomena at the working electrode surface is recorded. The current-potential response provides critical information about the electrochemical behaviour of the system, such as corrosion rates, passivation behaviour, oxidation and reduction reactions related to changes on the material or in the electrolyte and even catalytic activity. The recorded current is then plotted as a function of the applied potential, yielding a voltammogram. If the current is recorded in a range close to the OCP and plotted as a logarithmic function, that results in a Tafel plot, which is especially useful for the evaluation of corrosion rates. Similarly to OCP, factors such as surface roughness and cleanliness, material composition, temperature and type of electrolyte significantly affect the observed electrochemical responses. Also, the selected scan rate plays a role, since a faster scan rate can reveal kinetic limitations, while a slower scan rate allows for near-equilibrium conditions[26].

3.2.3. Cyclic Voltammetry

The Cyclic Voltammetry (CV) is a variation of the LSV. In a CV, the potential of the working electrode is swept linearly over time in one direction and then reversed to return to the initial potential, forming a cyclic sweep. The resulting current is recorded as a function of the applied potential, generating a cyclic voltammogram. Similarly to LSV, with CV measurements it is possible to investigate oxidation and reduction mechanisms, with the further possibility of identifying reversible and irreversible processes. Also, the evaluation of catalytic activity by observing shifts in peak potentials and changes in current density is feasible with CV. In this work, small-amplitude cyclic voltammetry measurements were used to normalise the active area of the WE, to directly compare the results of LSV. In fact, the area under the curve, normalised by the sweep rate, is proportional to the charge passing through the electrode. The charge, as it also happens in a capacitor, is proportional to the real electrode surface area, in turn. Due to surface roughness, the real and geometrical areas of an electrode never match. The measure of the charge is then a way to compare the real surface area of electrodes with different surface finishing if performed close enough to the OCP to avoid faradic reactions.

3.2.4. Potentiostatic Amperometry or Chronoamperometry

Contrary to LSV, in potentiostatic amperometry measurements (or chronoamperometry, CA), the potential at which the WE is polarised with respect to the reference electrode is kept constant for the duration of the measurement, while the resulting current, typically associated with oxidation or reduction processes, is monitored over time. This time-dependent current response can reveal information about electrode surface reactions, diffusion dynamics, and adsorption-desorption phenomena, as well as changes in the electrolyte concentration. In fact, CA is used to study corrosion inhibition mechanisms and passivation behaviour by observing how current stabilizes or decays under constant potential conditions. At the same time, by measuring current over time, charge transfer-limited and diffusion-limited processes can be distinguished as well as surface adsorption or desorption of ions, molecules and catalysis on the electrode surface. As for OCP, LSV and CV, CA investigations are also susceptible to sample surface finishing, electrolyte chemistry and measurement conditions.

3.2.5. Electrochemical Impedance Spectroscopy

Electrochemical Impedance Spectroscopy (EIS) measurements belong to the group of AC techniques, since an alternating current, defined by a sinusoidal wave shape, is over-imposed at a specific potential on the system of interest. As the name itself recalls, what is recorded and further used for subsequent calculations is the impedance response of the working electrode. Similar to the concept of resistance (R), that is the quantification of the opposition faced by a current (i) to flow between two points at a specific potential difference (E) in a direct current system, the impedance (Z) can be defined as the measure of the resistance that a circuit opposes to the flow of an alternating current. In the latter case, both current and electrical potential are frequency-dependent, with the frequency (ω) defined as the angular frequency of the oscillating sine wave perturbation overimposed on the investigated system and reported in units rad/s (equivalent to $2\pi f$ or Hertz (Hz)). As previously anticipated, the electrical potential of the working electrode is measured or applied with respect to the potential of a reference electrode, for example, an Ag/AgCl electrode. During potentiostatic EIS the applied potential perturbation can be described as in **Equation 7**.

Equation 7: $\mathrm{E(t) = E_0 cos\,(\omega t)}$

Where E_o is the amplitude of the overimposed sine wave amplitude, ω is the angular frequency, t is the time and the term ωt is known as the phase of the waveform. The monitored output current signal (i(t)) will have the same frequency as the input signal (ωt), but its phase will be shifted by a finite quantity (ϕ) defined as phase shift or phase angle, as represented in **Equation 8**.

Equation 8: $\mathrm{i(t) = i_0 cos\,(\omega t - \phi)}$

The measured output current of the system (i_0) will be inversely proportional to the electrochemical impedance of the system at the specific frequency. During EIS measurement, the amplitude of the sinusoidal signal is kept constant, while the frequency is varied in steps. Each frequency step is equally spaced on a logarithmic scale, usually comprehended between 1 MHz and 10 mHz. The collected data of potential vs. time and current vs. time for each frequency are treated via Fast Fourier Transform (FTT) by the potentiostat software. Such data manipulation gives back the potential magnitude vs frequency and current magnitude vs frequency, respectively. The magnitude of the impedance, |Z|, is equal to the potential amplitude E_o divided by the current amplitude i_0 as shown in **Equation 9**.

Equation 9: $\mathrm{|Z| = \frac{E_0}{i_0}}$

Commonly, data collected during EIS investigations are represented in the form of Bode and Nyquist plots. A Bode plot is produced by plotting the magnitude of the impedance |Z| and the phase angle φ as a function of the frequency on a double-axis plot, as shown in **Figure 4**.

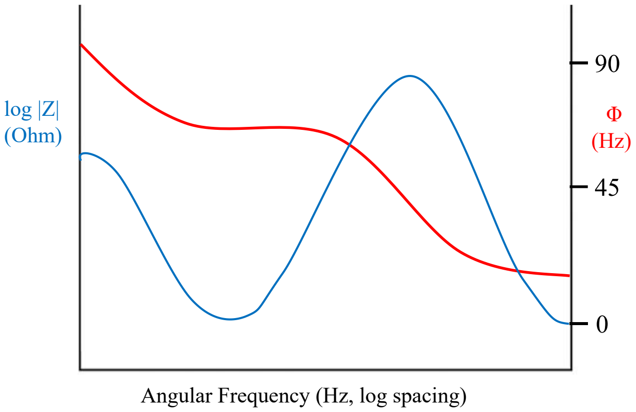

Figure 4: Example of a Bode plot[27].

To produce a Nyquist plot, the impedance magnitude |Z| can be intended as a vector characterized by a module equal to |Z| and an angle that is phase angle φ, as in **Figure 5a**. Cartesian coordinates may be used by breaking down the vector module (|Z|) into its x and y components[27], as presented in **Figure 5b**.

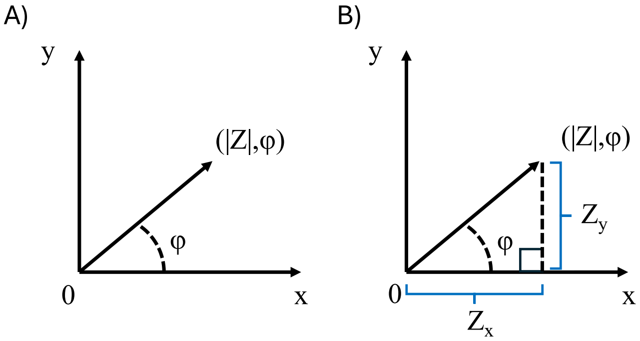

Figure 5: a) Representation of Z in polar coordinates, b) x and y components of Z.

Concerning Figure 5b, using trigonometry, it is possible to define the x and y components of Z, respectively Z_x and Z_y, as a function of the module and the phase angle, as reported in **Equation 10**, **Equation 11** and **Equation 12**.

Equation 10: $Z_x = |Z| \cos \phi$

Equation 11: $Z_y = |Z| \sin \phi$

Equation 12: $|Z| = \sqrt{(Z_x)^2 + (Z_y)^2}$

The obtained x and y components of the impedance's magnitude are addressed as real impedance Z_r and imaginary impedance Z_i, respectively. The reason is due to the mathematical treatment of equations 1 and 2 with Euler's formula to describe them using complex coordinates[2]. However, the trigonometrical simplifications reported above lead to the same conclusion and suffice for the aim of this introduction to EIS measurements. Plotting on the x-axis the real impedance Z_r (or Z^I) and on the y-axis the negative imaginary impedance $-Z_i$ (Z^{II}), the Nyquist plot (**Figure 6**) is finally obtained[27].

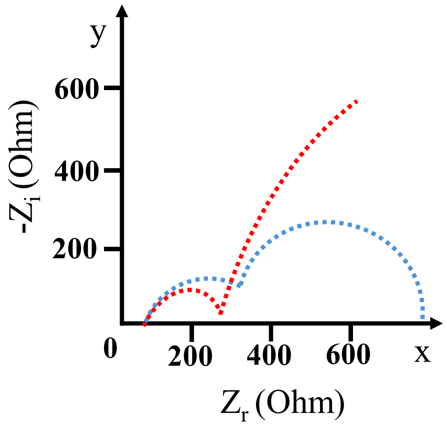

Figure 6: Examples of a Nyquist plot.

The reason why the Z_i are represented inverted is that the large majority of all Z_i are negative and doing so, it is possible to represent them in the first quadrant of the Cartesian plot.

3.2.5.1. Surface Oxide Thickness Calculation from EIS Data

Besides the real and imaginary components of the impedance, EIS measurements can, provide several useful information that can be exploited for further calculations. Some, as shown inFigure 7, are immediately accessible or require minor data manipulation and fitting.

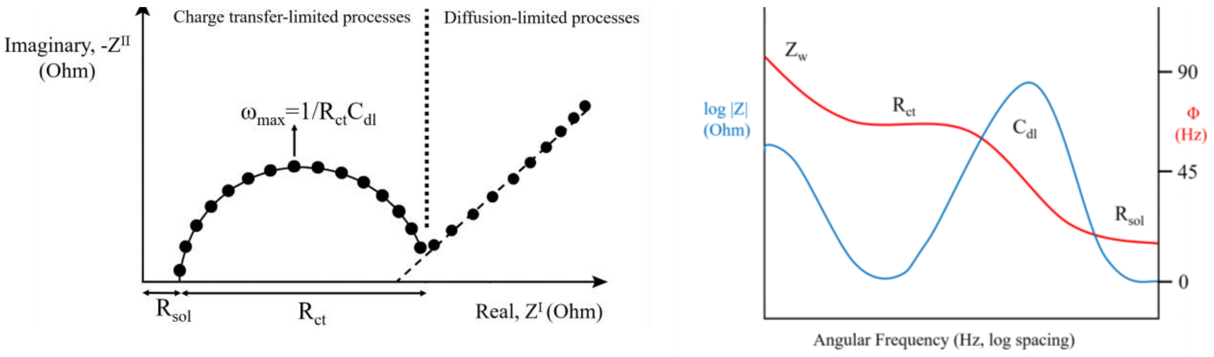

Figure 7: On the left: Nyquist plot. On the right: Bode plot. ω is the angular frequency (2πf), R_{ct} is the charge-transfer resistance, R_s is the resistance of the solution, C_{dl} is the double-layer capacitance, and Z_w is infinite diffusion.

Other characteristics of the investigated samples require some more calculations, such as the real capacitance, C_{real}, that can be defined as shown in **Equation 13**[28].

Equation 13: $$C_{real} = \frac{Z_{im}}{2\pi f\left(\left(Z_{real}-R_{sol}\right)^2-\left(Z_{im}\right)^2\right)}$$

In Equation 13, the capacitance of the sample (C_{real}, in Farad) is calculated starting from the values of Z_{im}, Z_{real} (in Ohm, respectively Z^{II} and Z^I) and the resistance of the electrolyte solution (R_{sol}, in Ohm), while f is the frequency applied during the measurement (in Hertz). **Equation 14** is then used to calculate the thickness of the scale.

Equation 14: $$Scale\ Thickness = \frac{A \cdot \varepsilon_0 \cdot \varepsilon_{oxide}}{C_{real}}$$

Where A refers to the geometric area of the sample, in m^2, exposed to the electrolyte (i.e., the WE). ε_0 and ε_{oxide} are the electrical permittivity (i.e., dielectric constant) values in the vacuum and in the oxide, respectively. The electrical permittivity values used in this thesis are shown in **Table 1**.

Table 1: Oxides considered for the calculations of the surface scale thickness and their electrical permittivity

Oxide	**Electrical Permittivity (F)**	**Source**
Cr_2O_3	11.8-13.3	[29]
ZrO_2	20-30	[30], [31], [32]
NiO	11-12	[33]

However, it has to be noted that none of the investigated alloys exclusively form a singular type of oxide on their surface, but rather mixed oxides or chromium- and/or nickel-rich spinels supported by chromia. This simplification of the actual composition of the surface scale is a necessary step due to the lack of data and complexity of compositions. Good correlations between the approximated values, calculated with the presented approach, and the real values have been proven in previous papers[28].

4. Experimental

4.1. Materials

4.1.1. Containers for Irradiation and H_2O_2 Reactivity Studies

The presented investigations have been performed using hydrolytic glass vials (Genetec, articles 20090873, 18090864) of a nominal volume capacity of 20 ml. The investigated septa were made of 1.5 mm thick, 55° shore A, white silicone rubber and red PTFE lining (Genetec, article 18032063), 3 mm thick, 45° shore A, translucent blue silicone and white PTFE lining (Genetec, article 20030163) and 3 mm thick, 50° shore A, white silicone and aluminium foil lining (Genetec, article 20030327). For clarity, the septa will also be respectively identified in the following graphs with the numbers 1, 2 and 3. The septa were respectively accommodated in 18 mm magnetic universal screw caps with a central hole and 20 mm aluminium crimp caps with a central hole.

4.1.2. Alloys

All the investigated alloys, except AISI 441, were provided by Westinghouse Electric Company LLC, in Västerås. The samples were sourced from their workshop. The AISI 441 samples were sourced by Alleima. The generic elemental composition of the tested alloys is reported in **Table 2**.

Table 2: Elemental composition of the investigated alloys in weight percentage ($\%^{wt}$).

Material	Fe	Ni	Zr	Cr	Ti	Mn	Nb	Sn	Al	Cu	Co	Mo
AISI 441	Bal.			17.5-18.5	0.1-0.6	1.0	0.5-1.0					
Inconel 718	11.6-22.7	Bal.		17.0-21.0	0.8-1.15	0.35	4.8-5.2		0.4-0.6	0.23	1.0	2.8-3.3
Inconel X-750	5.0-9.0	Bal.		14.0-17.0	2.25-2.75	1.0	0.7-1.2		0.4-1	Max 0.5	max 1.0	
Zry-2 Low alloy	0.07-0.2	0.03-0.8	Bal.	0.05-0.15				1.2-1.7				
AISI 316L	Bal.	10-13		16.5-18.5		2.0						2.0-2.5

The materials were provided in the form of foils, with thicknesses varying between 0.2 to 0.8 mm. The foils were cut into coupons of dimensions 2 x 1 cm with a manual guillotine for metal sheets to use them for the experiments. Before performing any test, samples' edges were ground with 1200 grit SiC sandpaper (Struers) to remove any burrs. Subsequently, they were cleaned with an ultrasound bath in acetone (Sigma Aldrich) and then Ethanol (Sigma Aldrich) for 10 minutes each, 2 times. From now on, in this thesis the samples prepared as just described will be called “as-received”. For some specific experiments, all the faces of the coupons were ground with 500 grit SiC sandpaper (Struers). From this point, samples whose all surfaces were ground will be addressed as “ground”.

4.2. Setup for Irradiation and H_2O_2 Concentration Measurements

The irradiations were performed by placing the samples in the exposure chamber of a shielded irradiator (Gammacell 220) equipped with cobalt-60 sources. Prior to the irradiation campaigns, the γ-dose rate was measured by chemical dosimetry (Fricke dosimetry) in different locations of the irradiation chamber to ensure that homogeneous irradiation of the samples was achieved. The dose rate was measured to be 3.6 kGy/h in June 2022. The received doses of the samples were tuned by varying the irradiation time, knowing the dose rate in the irradiation chamber. The irradiation times were also adapted to the reduced activity of the source over time, to compensate for that.

The water used for all the investigations was Milli-Q® water produced with in-house equipment. All the samples were sealed under an ambient atmosphere once filled with 15 ml of solution. For the samples subject to multiple sampling, at precise time (dose) intervals during the irradiation, 1 ml disposable syringes (disposable luer-slip two-parts tuberculin syringe, Fisher Scientific) equipped with disposable 25x0.5 mm needles (Braun) were inserted through the septa to withdraw a volume of the irradiated solution. The collected volume, between 0.1 and 0.2 ml, was transferred into a microtube (Eppendorf Snap Cap, 1ml) and then used for H_2O_2 concentration measurements.

For the investigation of alloys-assisted H_2O_2 degradation and the electrochemical investigations, H_2O_2 solutions, created from Milli-Q water (<18MΩ) previously irradiated in-house, were diluted to the desired final concentrations of 0.10 and 0.15 mM. This was done to avoid the influence of stabilisers usually present in commercially available H_2O_2. All the hydrogen peroxide solutions with a concentration above 1 mM were prepared starting from 15 % H_2O_2 sourced from Nouryon before the addition of stabilisers.

The H_2O_2 concentration was assessed by the triiodide method: 1 M potassium iodide solution (Sigma-Aldrich) was freshly prepared and mixed with a pH 4.65 acetate buffer (Sigma-Aldrich) solution spiked with ammonium molybdate tetrahydrate (Sigma-Aldrich) and milli-Q water immediately before adding the sample in a volumetric ratio of 1:1:18:0.5 This precaution was taken to prevent ageing phenomena that could potentially alter the experimental results. For the same reason, absorbance measurements were performed shortly after their preparation. The photometric measurements were performed using a Varian Lambda 25 and a VWR UV3000 UV-Vis spectrophotometer. Before any investigation, the absorbance extinction coefficient for I_3^- was calculated, measuring the absorbance of different dilutions of known amounts of H_2O_2 (Eka HP). The solutions were also titrated with potassium permanganate ($KMnO_4$, Sigma Aldrich) with a software-controlled titrator (Titrando 907, Metrohm). The Absorption extinction coefficient at 350 nm was calculated to be $2.38*10^4$ l mol^{-1} cm^{-1}, well in agreement with various published values ranging between

$2.32*10^4$ l mol^{-1} cm^{-1}[34] and $2.40*10^4$ l mol^{-1} cm^{-1}[35]. Absorbance measurements were performed at 350nm in single-beam mode, manually subtracting the absorbance of the blank sample before data plotting. The same quartz cuvette was used for all the measurements.

4.2.1. Electrochemical Measurements, EIS

The electrochemical measurements presented in this work have been performed with a SP300 potentiostat-galvanostat by BioLogic. The instrument was controlled by a computer, through the Biologic software suite EC-lab V11.61. All the investigations were performed in 1%^{wt} sodium sulfate (Na_2SO_4, 70 mM). EIS measurements were carried out in a custom-made well-type electrochemical cell, as represented in **Figure 8**. This specific cell design allows for testing of only one side of the sample, avoiding interferences from the edges and the back side of it, facilitating the control of the active area. For the measurements performed outside of the irradiation chamber, a commercial 3M KCl Ag/AgCl reference electrode (Sigma Aldrich) and a platinum counter electrode were used.

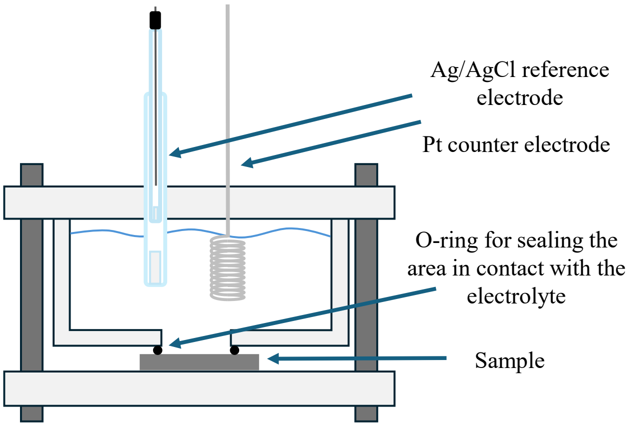

Figure 8: Cross-section of the custom-made electrochemical cell used for the EIS investigation of the samples.

All potentiostatic EIS measurements were performed at the OCP, previously measured until stabilization, in the range of frequencies between 1 MHz and 30 mHz. The amplitude of the overimposed sinusoidal excitation was 10 mV. Investigations were performed in an air-saturated, 1 %^{wt} Na_2SO_4 electrolytic solution.

4.2.2. Design and Assembly of Reference Electrode and a 3D-Printed Electrochemical Cell

The investigation of samples during irradiation requires specific precautions to prevent or limit possible biases and produce reliable, consistent measurements. First, all the materials of the electrochemical cell must be radiation-resistant. This is to prevent contamination of the electrolytic solution with the byproduct of materials' degradation under irradiation. Therefore, the EC cell presented above was dismissed, due to the perturbations that both the sealing O-ring and the PTFE walls could have had.

The use of a glass beaker was therefore preferred. In order to perform an electrochemical measurement, the electrolyte has to be in contact only with the surface of the WE, and not the electrical contacts (e.g., crocodile clamp, copper wires, etc.) used to connect it the EC setup.

Given the availability of a Fuel Deposition Modelling (FDM) 3D printer, an inexpensive electrode holder in a CAD software (SolidWorks 2021, Dassault Systèmes) was designed to be placed it on top of the beaker, as shown in **Figure 9**. The holder, printed in Polylactic Acid (PLA) is characterised by three equidistant, circumferential holes. Such holes are thought to accommodate adaptors (3D-printed too) to firmly keep in position the three electrodes, whatever their size or shape. For the realization of EC measurement in inert atmosphere, a flexible tube fed with Ar gas was positioned through the central hole. The argon gas was then bubbled in the electrolytic solution for at least 1 hour to effectively remove O_2. During EC investigation, to prevent the disturbances that a bubbling solution would have had on the measurements, the tube was lifted and Ar gas was blown on the surface of the solution instead. During the use of Ar gas, the other unused apertures of the electrode holder were sealed with Parafilm® with the exception of a small passage, to prevent the ingress of air and the buildup of excessive argon overpressure in the headspace.

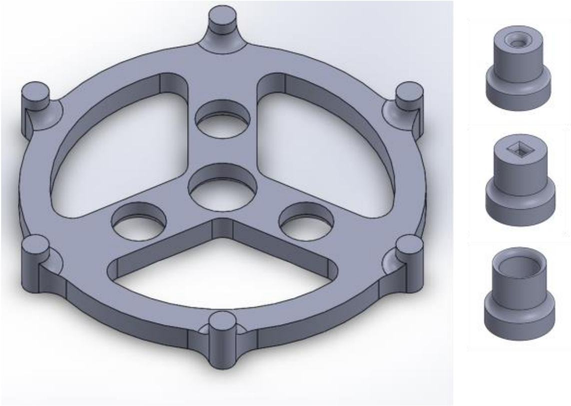

Figure 9: CAD model of the electrode holder and the adaptors.

To solve the problem regarding the control of the WE's surface area exposed to the electrolytic solution, and therefore electrochemically active, the design of the sample coupons was changed. Instead of the 2 x 1 cm standard dimensions used for all the investigations, 3 cm by 1 cm samples were prepared. A 2.5 mm hole was then drilled close to one of the two extremities on each of them. In one of the printed adapters was then accommodated a strip of copper foil, 2 mm by 1 mm in section and ca. 5 cm long, with the extremity facing the inner volume of the beaker (now turned into an EC cell) bent upward to form a hook. During the EC investigation, the samples were then hung by the copper hook, to which the WE cable was clamped on the upper facing extremity, with the electrolytic solution covering only the bottom 2/3 of the samples. All the samples for this part of the investigation were of the ground-type.

4.2.2.1. Counter Electrode and Irradiation

As the rest of the EC cell, the reference and counter electrodes are also irradiated during the measurements. During preliminary tests, the Pt counter electrode left submerged in a 0.1 mM non-stabilised H_2O_2 solution alone reduced its concentration by 13% in 3 h. The same test, repeated under irradiation, highlighted how the hydrogen peroxide concentration build-up due to radiolysis was slowed down, due to the catalytic consumption of H_2O_2 on the Pt surface. Further tests using a graphite rod have shown no alteration of H_2O_2 concentration over the same period and H_2O_2 build-up rate close to the reference sample under irradiation. Graphite was then the material of choice for the CE.

4.2.2.2. Assembly of a Radiation-Resistant Reference Electrode

It is known from the literature that Ag/AgCl electrodes perform satisfactorily under gamma irradiation, even at high temperature and pressure[36]. However, commercial reference electrodes have multiple parts (e.g., frit, frit connection, upper seal, etc.) made of polymers and resin. During the preliminary test of the setup, criticalities have arisen with different commercial electrodes. Unstable potentials, poor or intermittent electrical connection, and spikes in the current were indications that the polymeric parts of the RE were degrading due to irradiation and compromising the functionality of the electrodes themselves. A full-glass electrode, shown in **Figure 10**, was then assembled in-house.

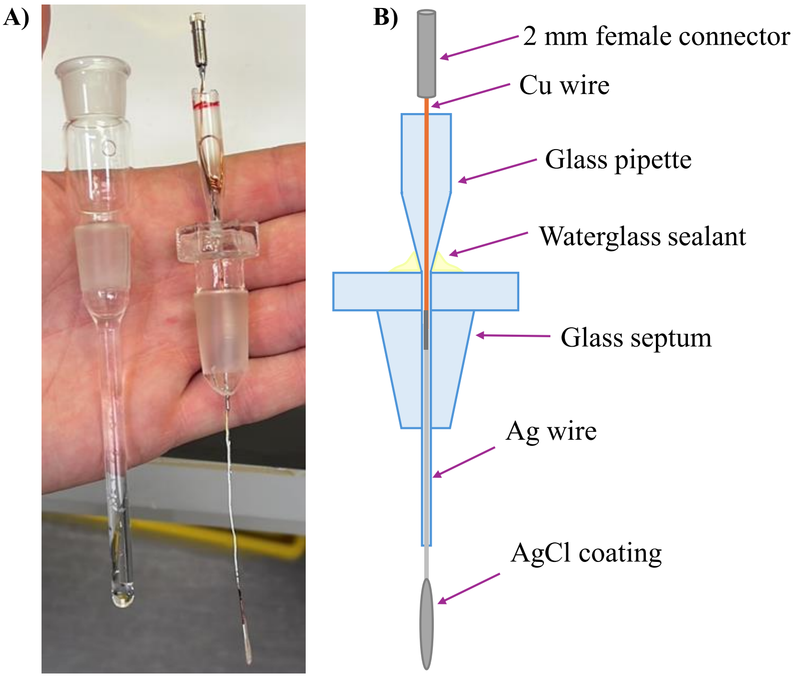

Figure 10: A) Self-assembled, full glass, Ag/AgCl electrode. Left: glass tube bridge, later filled with 3M KCl solution. On the right: the inner structure with the AgCl-covered silver filament. B) Schematic representation of the reference electrode.

A silver filament covererd with AgCl was inserted into a shortened glass Pasteur pipette, leaving the portion covered in AgCl deposit protruding out of it. A copper wire of suitable diameter had one extremity covered in tin and inserted from the larger opening of the glass pipette until in contact with the Ag filament. A gas-fired blow torch was then used to melt the glass and seal the two wires in it, soldering the two at the same time. The as-obtained core was then inserted through a glass stopper (carefully drilled with a Dremel tool and diamond bits) of dimensions suitable to fit in a glass bridge tube. The opening at the bottom of the stopper was sealed melting once more the glass with the torch. The upper opening, since not supposed to be in contact with any liquid, was sealed using a sodium trisilicate (water glass, $(NaOH)_x(Na_2SiO_3)_y{\cdot}_zH_2O$) solution. Finally, a 2 mm plug connector (Hirsher) was soldered at the end of the copper wire, and the glass bridge tube was filled with a 3M KCl (Sigma Aldrich) solution. The assembled RE was tested vs a new RE (modular reference system, Ag/AgCl, 6.0724.140, Metrohm) and proved its reliability, with a maximum discrepancy of 0.3 mV.

5. Results and Discussion

5.1. Irradiation of Septa and H_2O_2 Consumption Over Time

The H_2O_2 concentration measured in aqueous solutions contained in glass vials irradiated up to 250 kGy is plotted vs the received dose in **Figure 11**. The vials were sealed by three different types of septa (i.e., white silicone rubber/red PTFE, blue silicone rubber/white PTFE and white silicone rubber/Al lining). Both sides of the septa were tested facing the headspace, for a total of six samples that were irradiated simultaneously. During irradiation, the vials were kept in upright position, preventing the direct contact of the solutions with the septa.

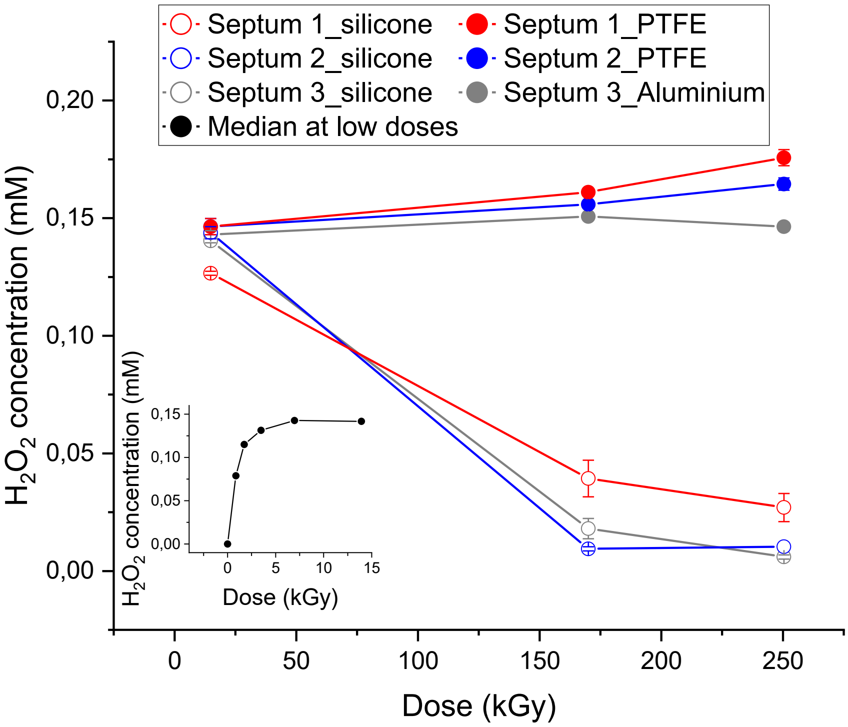

Figure 11: Measured H_2O_2 concentration versus received dose for the six irradiated samples, three for each type of septa facing the vial (septum 1, red: red PTFE/ white silicone rubber, septum 2, blue: PTFE/blue silicone rubber and septum 3, grey: aluminium/white silicone rubber). Hydrogen peroxide concentration measurements were performed at 14.8, 170 and 250 kGy received dose intervals. In the inset: the median of the H_2O_2 concentration measured at lower doses (between 0 and 13.9 kGy).

The measured concentrations of hydrogen peroxide in the six samples are comparable up to an absorbed dose of 14.8 kGy, ss visible in **Figure 11**. At 250 kGy, however, the samples can be clearly categorised into two distinct groups based on their H_2O_2 content. Specifically, the samples sealed with aluminum (Al) and polytetrafluoroethylene (PTFE) linings in contact with the headspace exhibit H_2O_2 concentrations ranging from 0.16 to 0.19 mM. In contrast, samples sealed with silicone rubber septa exhibit markedly lower concentrations, approximately 0.02 mM, representing only 10.5% to 12.5% of the concentrations observed in samples sealed with Al and PTFE septa. These findings indicate that the divergence in H_2O_2

accumulation begins to emerge between 14.8 and 170 kGy, with no appreciable differences detected at lower doses (0–14.8 kGy).

To determine whether the observed variations are attributable solely to the sealing material or also to its exposure to the gaseous headspace, a second series of experiments was conducted in which the vials were inverted. This configuration placed the septa in direct contact with the aqueous solution while isolating the gaseous headspace from the sealing material, which was instead in contact with the glass. The results of these inverted-vial experiments are presented in **Figure 12**. Throughout the entire duration of this series, the vials were maintained in the inverted position to ensure continuous contact between the sealing septa and the contained solution.

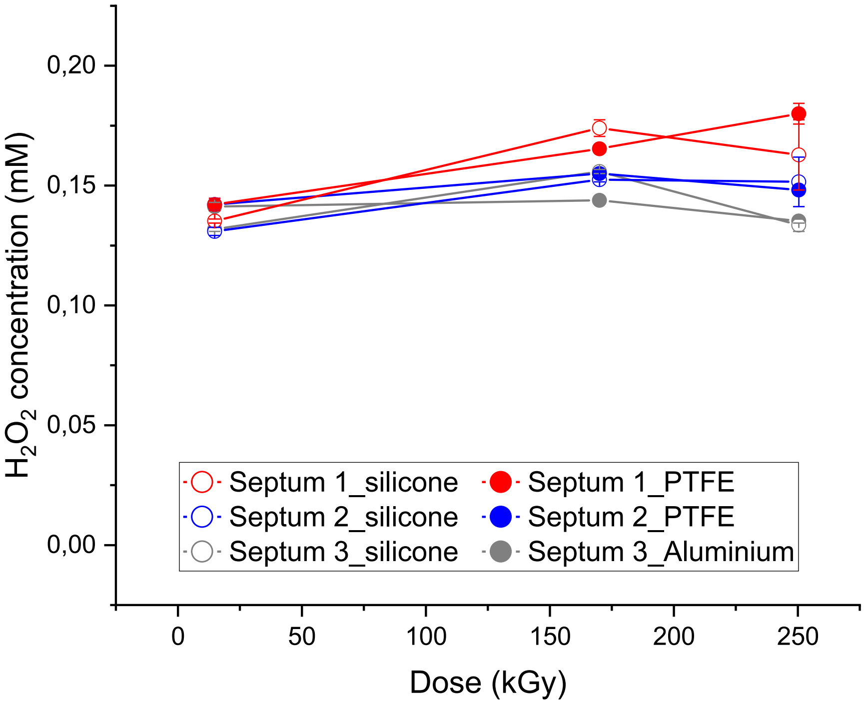

Figure 12**:** H_2O_2 concentration versus absorbed dose for the six irradiated samples, two for each type of septa facing the vial (septum 1, red: red PTFE/ white silicone rubber, septum 2, blue: PTFE/blue silicone rubber and septum 3, grey: aluminium/white silicone rubber). Hydrogen peroxide concentration measurements were performed at 14.8,170 and 250 kGy. Samples were kept in the upside-down position for the whole duration of the experiment.

As can be seen in **Figure 12**, when the vials are placed upside-down and the materials are in direct contact with the solution, the difference observed in **Figure 11** is no longer present. Hence, the impact of silicone in contact with the inner environment of the vials is only seen when it is in contact with the headspace. Subsequently, H_2O_2 concentration was monitored in the absence of γ-radiation after 28 days, to explore the hydrogen peroxide reactivity towards the investigated septa materials. The results are presented in **Figure 13**.

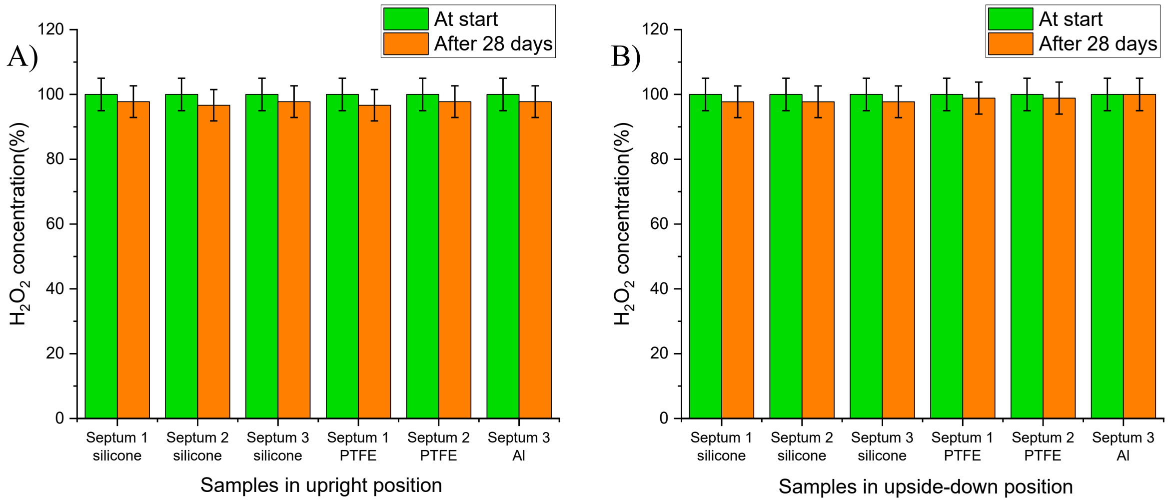

Figure 13: A) Relative H_2O_2 concentration of the six investigated samples, three for each kind of septa kept in the upright position for the entire duration of the test. B) Relative H_2O_2 concentration of the six investigated samples, kept in the upside-down position for the entire duration of the test. Vials were filled with 0.15 mM H_2O_2. In green, the H_2O_2 concentration was measured at the beginning of the test. In orange, the H_2O_2 concentration was measured after 28 days.

To prevent possible biases due to the presence of stabilizers (commonly found in commercially available H_2O_2) in the experiment, we made use of radiolytically produced hydrogen peroxide. Over the investigated period of 28 days, none of the septa, either kept in the upright or upside-down position, exhibited any significant reactivity towards H_2O_2, as clearly shown in **Figure 13**. A minimal decrease in hydrogen peroxide content is expected, given the inherent instability of H_2O_2 and the lack of preservatives. Therefore, it is evident that the phenomena observed in **Figure 11** and **Figure 12** cannot be simply attributed to the reactivity of H_2O_2 toward the tested materials.

As shown above, a reduction in H_2O_2 concentration is observed only when silicone rubber faces the gaseous headspace, not when it faces the solution or when PTFE or aluminium is used in similar configurations. Reactivity tests confirm that H_2O_2 does not directly react with any of the materials tested. Upon irradiation, silicone forms carbon-centred radicals that readily react with molecular oxygen (O_2). Since the O_2 concentration is significantly higher in the headspace than in the aqueous phase (by a factor of ~30), our hypothesis is that radical–O_2 reactions proceed faster when silicone is exposed to the gas phase. This rapid O_2 consumption drives further depletion of dissolved O_2 due to equilibrium shifts, reducing H_2O_2 formation, as O_2 is a known precursor. When silicone faces the solution, this effect is minimised due to lower radical–O_2 reaction rates and fast O_2 replenishment from the headspace.

These findings represented an important achievement for the development of a reliable experimental methodology for the project, shining a light on aspects often overlooked that, as demonstrated, can heavily influence the experimental conditions and thereby the outcome of the experiment.

5.2. Irradiation of Alloys and H_2O_2 Consumption Over Time

Once the optimal experimental conditions for the study of H_2O_2 accumulation and stability (e.g., vials and caps able to withstand high gamma doses and not to alter hydrogen peroxide build up) were identified, coupon samples of the alloys were irradiated in sealed vials filled with water, as described in detail in 4.1. H_2O_2 concentration was monitored at dose intervals of 85, 550, 1100, 1650 and 2200 kGy, as shown in **Figure 14.** Both samples of as-received (henceforth called A.R., **Figure 14 A**) and ground (**Figure 14 B**) alloys were independently irradiated. The choice of investigating the materials in both surface conditions results from the intention of testing surfaces covered by very thin oxides and of minimizing morphological and chemical differences between samples. Since sourced from the factory, the A.R. form is the closest to the actual state of the alloy when transformed into parts of a NPP. At the same time, given their origin, their surface finishing may not be homogeneous (e.g., scratches, deformations, thermal alterations, etc.). The grinding process, removing the outermost layer, exposes new material, creating a more uniform starting condition for all the samples. From the H_2O_2 measurements, it is immediately visible how the composition of the alloy affects the long-term concentration of radiolytically produced hydrogen peroxide. Despite a significant spread for some datapoints of certain samples (due to the alteration of the atmosphere in the headspace during the multiple sampling performed and the possible introduction of fragments of the septa material, as happened for the ground sample of Inconel X-750, **Figure 14 B**), some trends can be identified.

The H_2O_2 concentration in the solutions containing AISI 441 alloy is consistently lower than that of the other alloys. Hydrogen peroxide content seems to start decreasing after receiving 0.55 MGy. In bare water, the concentration of H_2O_2 reaches up to 0.26 mM, following a steadily increasing trend, as in figure **Figure 14 A and B**. Solutions containing Zircalloy samples behave more similarly to bare water, indicating low reactivity involving such metallic samples. The solutions hosting Inconel 718 alloy samples show diminished hydrogen peroxide concentration in comparison to bare water and Zircalloy. The H_2O_2 concentration vs received dose trend seems to go from increasing to decreasing between 1.1 and 1.65 MGy, approaching what is observed for AISI 441. Inconel X-750 seems to behave similarly to Zircalloy in the A.R. state. However, as anticipated, Inconel X-750 is affected by larger uncertainties in its ground surface finishing.

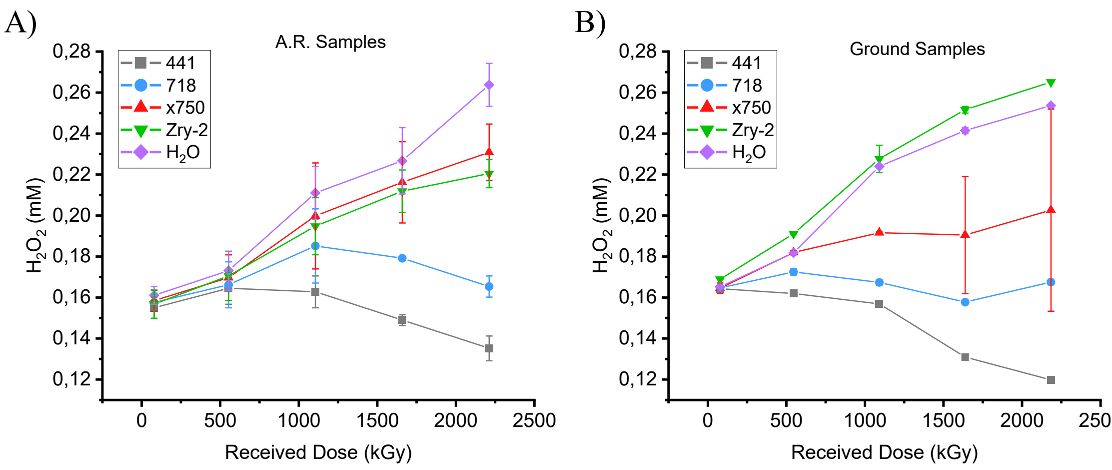

Figure 14: H_2O_2 concentration vs received dose for: A) as-received, A.R. and B) ground alloy samples. The points identified as "H_2O" refer to the vials containing only water with no alloy coupons submerged in the solution. The sampling was performed at received dose intervals of 85 kGy, 550 kGy, 1.1, 1.65 and 2,200 MGy

To prevent alteration of the irradiation conditions due to the recurrent sampling, the experiments were repeated, measuring hydrogen peroxide concentration only at the end of the irradiation (i.e, at a total dose of 2.2 MGy). The measured H_2O_2 concentration for the investigated alloys is presented in Figure 15 for both as received (A) and ground (B) samples.

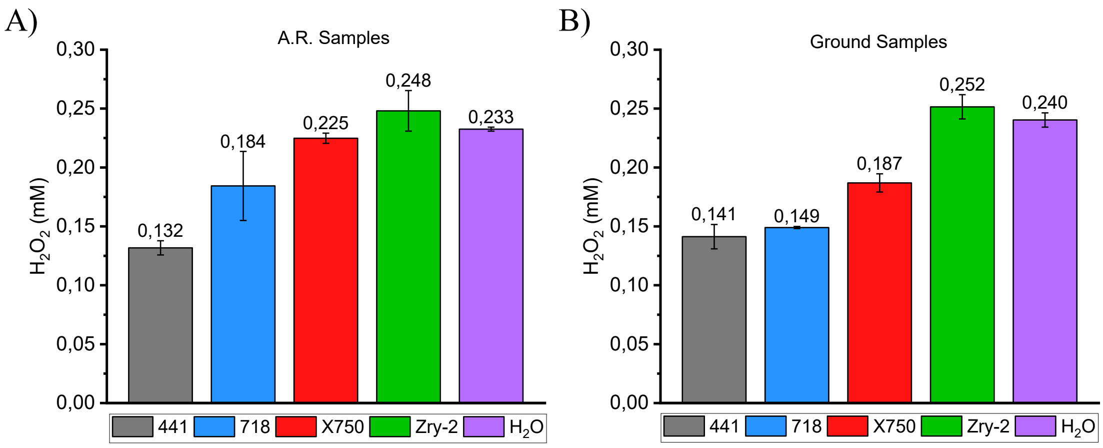

Figure 15: H_2O_2 concentration, in mM, of the irradiated water solution containing A) as received, A.R. and B) ground alloy samples. The samples identified as "H_2O" refer to the vials containing only water; no alloy coupons were submerged in the solution. The received dose at the time of the sampling was 2.2 MGy.

As is noticeable comparing **Figure 14** and **Figure 15**, the overall H_2O_2 yields seem to be confirmed. Zircalloy samples do not greatly affect the hydrogen peroxide concentration in the solution with respect to the bare irradiated water; on the contrary, they seem to slightly but consistently increase H_2O_2 final concentration, even if still within the uncertainty of the method. AISI 441 alloy induces a final hydrogen peroxide concentration of around 40% of the reference sample, independently of the surface finishing. Inconel alloys seem to be the most affected by the different surface finishing, with a stronger limiting effect on the H_2O_2 build-up in their ground conditions. Such a phenomenon could be an effect of both different surface composition and the greater area in contact with the solution.

To investigate whether the different hydrogen peroxide concentrations among samples were due to intrinsic characteristics of the alloy or induced by gamma irradiation, a reference test without irradiation was performed. The samples were left submerged in a 0.15 mM H_2O_2 solution for 28 days, which is the time extent necessary to reach the received dose of 2.2 MGy of the previous experiment. The hydrogen peroxide concentration measured for the different samples after 28 days is presented in **Figure 16**.

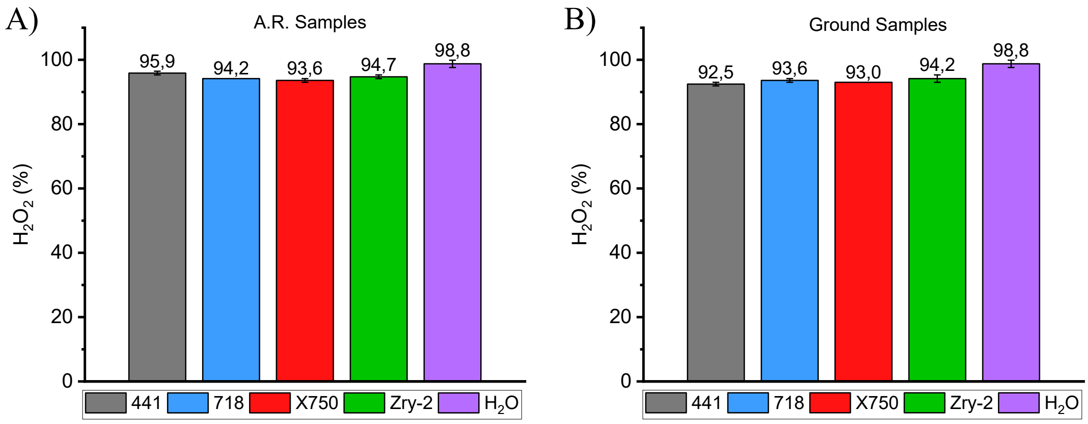

Figure 16: H_2O_2 concentration, expressed in % concerning the original content of 0.15 mM, for A) as received, A.R. and B) ground alloy samples. The samples have spent 28 days submersed in the solution before the concentration measurement.

According to the H_2O_2 consumption measurements presented in **Figure 16**, the reactivity of the same toward the investigated samples is not as great as under irradiation. Due to its inherent instability, H_2O_2 concentration is spontaneously reduced by 1.3% over 28 days. The solution in contact with AISI 441, Zircalloy-2 and Inconel samples lost between 5 to 6 % of the original H_2O_2 concentration. That accounts for about 4-5 % more than the spontaneous decomposition happening without contact with the metals. A minimal increase in H_2O_2 reactivity can be noticed for the ground samples with respect to the A.R. and could be explained by the larger sample area exposed to the solution. In general, the reactivity of hydrogen peroxide under the test conditions is minimal for all the alloys and the trends observed under irradiation are not reproducible for the as-received samples.

For a better understanding of the occurring phenomena, more samples were irradiated without sealing the vials, to allow air recirculation and unlimited oxygen availability. The experiment was performed in more recent times, hence under lower dose rate conditions, which in turn led to lower H_2O_2 concentrations. The hydrogen peroxide concentration measured at a received dose of 2.5 MGy are shown in **Figure 17**.

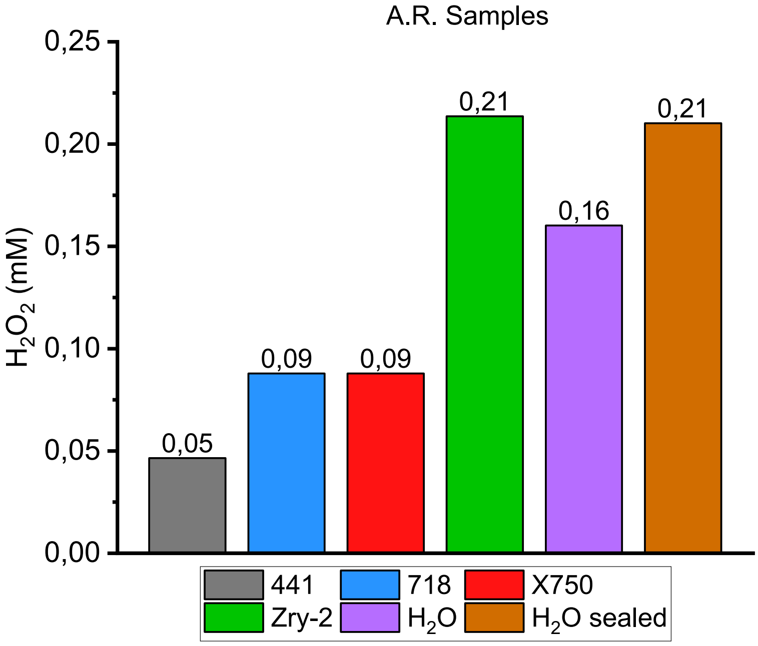

Figure 17: H_2O_2 concentration, in mM, of the irradiated water solution containing as received, (i.e., A.R.) alloy samples in open vials. The samples identified as "H_2O" refer to the vials containing only water; no alloy coupons were submerged in the solution. The received dose at the time of the sampling was 2.5 MGy. The graph lacks error bars since the repetition of the experiment has not been performed yet. However, the uncertainty of the presented data could be estimated to be within 5 %, considering instrumental accuracy and the operator's influence.

Under the abovementioned irradiation conditions, the H_2O_2 concentrations follow the trend outlined in **Figure 15** but differences between samples are escalated. AISI 441 alloy strongly affects H_2O_2 build-up, with its concentration stopping at only 22 % of the one achieved by the sealed reference ("H_2O sealed, brown colour) and Zircalloy samples. Both Inconel 718 and X-750 samples strongly affect H_2O_2 final concentration, but differently from the tests with sealed vials (**Figure 15**), there is no difference between the two alloys. Surprisingly, the hydrogen peroxide formed in the sealed reference vial is remarkably more than in the open reference vial ("H_2O, purple colour). Such a result is unexpected since the higher oxygen availability of the open vial should generate more H_2O_2 than in the sealed one. A possible explanation could be that impurities, such as Fe oxide powder originating from the chamber ceiling, contaminated the solution despite the precautions taken (i.e., shielding of the samples and thorough cleaning of the chamber prior to the experiment).

To investigate whether a greater thickness of the oxide scale could influence the hydrogen build-up under irradiation, samples of AISI 316L alloy have been heat-treated in a tube furnace in air atmosphere at 800° C for different time extents, leading to different oxide thicknesses and, conceivably, surface morphology and chemical compositions too. Subsequently, the samples have been submersed in water and irradiated with gamma radiation. H_2O_2 concentrations were measured at a received dose of 1 MGy and are shown in **Figure 18**.

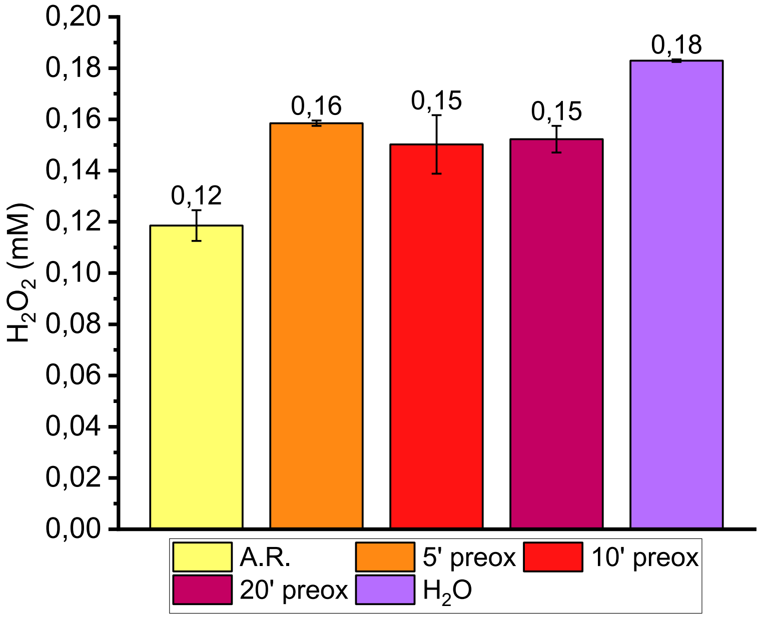

Figure 18: H_2O_2 concentration, in mM, of the irradiated water solution containing AISI 316L alloy samples, as received and pre-oxidized at 800 °C for 5, 10 and 20 minutes. The samples identified as “H_2O” refer to the vials containing only water; no alloy coupons were submerged in the solution. The received dose at the time of the sampling was 1 MGy.

As visible in **Figure 18**, the thermal treatment, and hence the progressively increasing thickness of the oxide scale, seems not to affect the long-term hydrogen peroxide concentration, with the three samples achieving very similar values. However, the amount of H_2O_2 found in the solution hosting the as-received sample is 25 % less than for the pre-oxidised samples, indicating a possible correlation between the thickness of the surface oxide and/or composition/morphology and their influence on H_2O_2 accumulation under irradiation.

5.3. Surface Investigation of Irradiated Alloys

As shown in **Figure 16**, we know that H_2O_2 reactivity without irradiation is very low. However, we cannot assume yet that the behaviour of hydrogen peroxide is the same also under irradiation. Therefore, SEM investigations were performed on both as-received and subsequently irradiated samples to assess the effect of gamma irradiation and exposure to water radiolysis products on the surface of the alloys. The samples depicted in **Figure 19, Figure 20, Figure 21** and **Figure 22** are the same object of the irradiation and subsequent H_2O_2 measurements of **Figure 15 A**. Considering the volume of the irradiated water samples, the final concentrations of H_2O_2 (presented in 5.2), and assuming that the difference, relative to the reference, was consumed in surface oxidation reactions on the alloys, the resulting oxide scale thickness would be expected to range from a few hundred nanometers to approximately one micrometer. This broad range is attributed to simplifications in the calculation, variability in the measured H_2O_2 concentrations, and assumptions regarding the composition of the oxide scale.

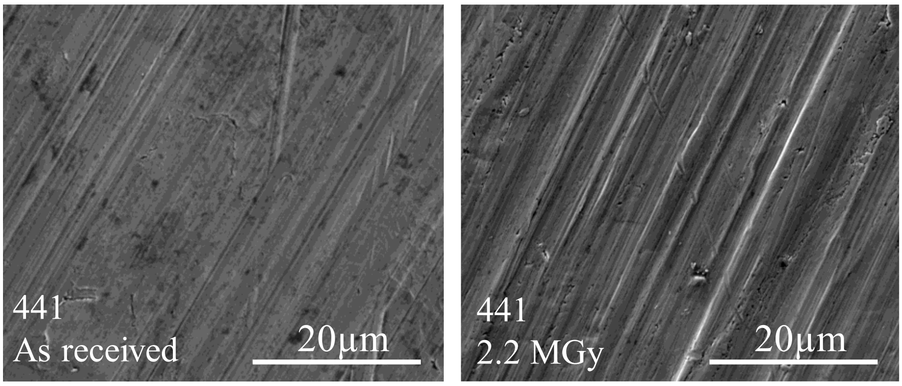

Figure 19: Surface SEM micrograph of A) as received, not irradiated and B) as received, irradiated AISI 441 samples.

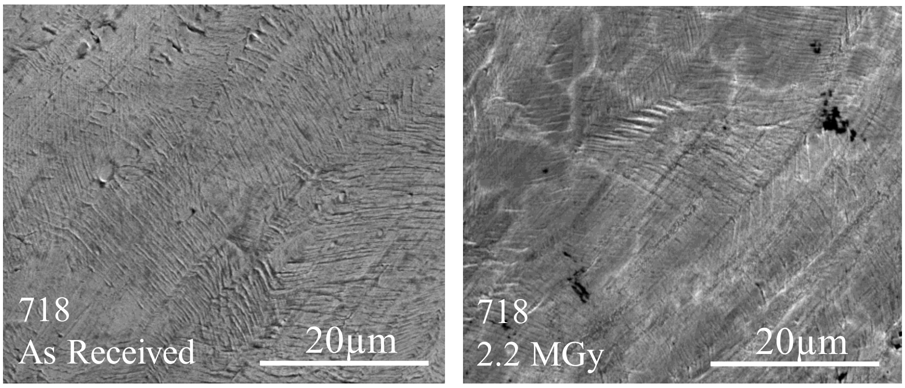

Figure 20: Surface SEM micrograph of A) as received, not irradiated and B) as received, irradiated Inconel 718 samples.

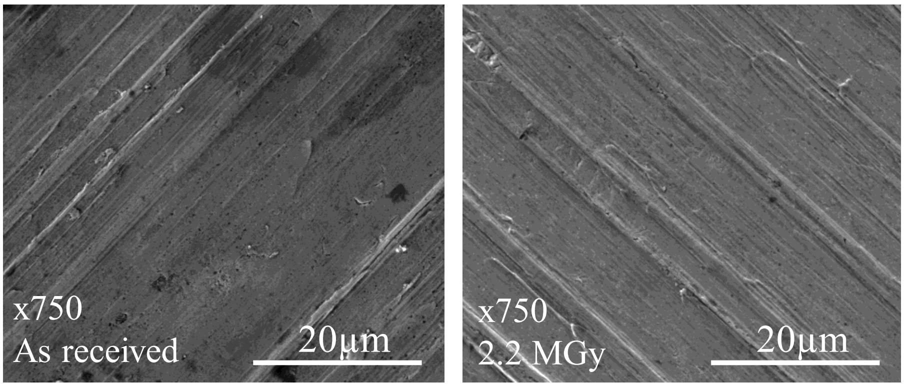

Figure 21: Surface SEM micrograph of A) as received, not irradiated and B) as received, irradiated Inconel X-750 samples.

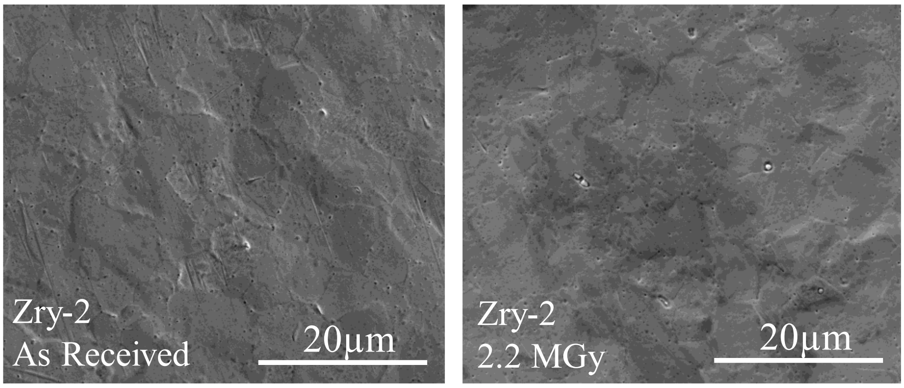

Figure 22: Surface SEM micrograph of A) as received, not irradiated and B) as received, irradiated Zircalloy-2 samples.

As visible in all the SEM micrographs presented above, the surface of the alloys seems unaffected by the irradiation and the simultaneous exposure to the product of water radiolysis. Features such as the ridges resulting from the surface finishing of the alloys (**Figure 19, Figure 21**) and even grain boundaries (**Figure 22**) are visible on the samples both before and after irradiation. Such features are not compatible with the expected oxide, calculated according to the abovementioned reasoning. Only a few minor differences are identifiable between micrographs and could be justified by the normal differences among areas of the same sample (especially considering their "as-received" condition), slightly different setting of the instrument and so forth.

However, it is not possible to exclude that the treatment has altered the oxide thickness on a scale below the appreciation threshold granted by SEM investigation of the surface (e.g., in the order of a few nanometers). For such a reason, a complementary investigation of the samples has been performed with XPS, which allows a greater sensitivity to the very surface of the samples as the depth of the interacting volume ranges between 5 to 10 nm. XPS analysis of the samples, conducted on as-received samples before and after irradiation, as well as after submersion in a H_2O_2 solution, is presented in the following figures. The samples labelled with "reference" in their names are untreated. Those labelled with "Gamma" and "H_2O_2" are irradiated up to 2.2 MGy (same samples investigated above) and submerged in a 1 mM solution of H_2O_2 for 28 days.

The High-resolution XPS spectra for the AISI 441 samples, presented in **Figure 24,** confirm that the three samples share a very thin surface oxide layer, with the signals of the metallic iron and chromium still clearly visible and accounting for between 21 and 24 % of the total signal of Fe and 18 to 20.5 % of that of Cr. The counts for the peaks of the reference (i.e., as-received) sample and the one submersed in H_2O_2 differ by less than 1% for both Fe and Cr. The irradiated sample contains slightly more oxidised iron, less than 3%. Considering the depth of the interaction volume investigated through XPS (i.e., between 5 to 10 nm), the differences between samples are minimal, and the oxides could be judged equally thick or with differences not exceeding 1 nm.

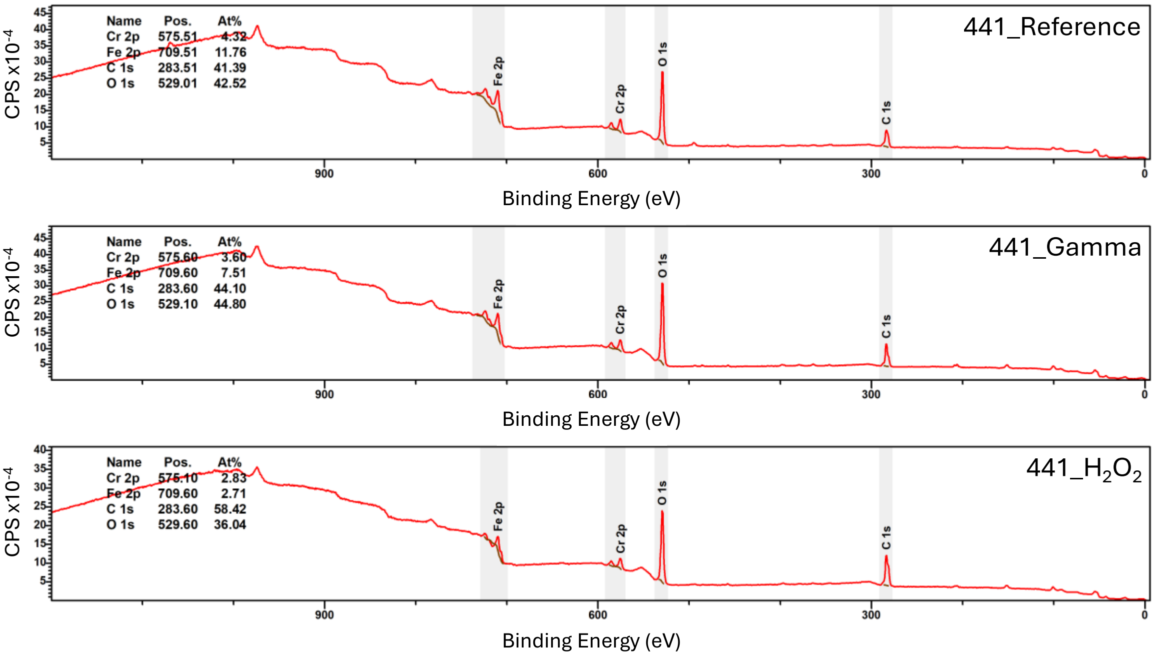

Figure 23: XPS wide spectra collected for the AISI 441 alloy samples: as-received (top), irradiated up to 2.2 MGy in water (centre) and submersed for 28 days in a 1 mM solution of H_2O_2 (bottom).

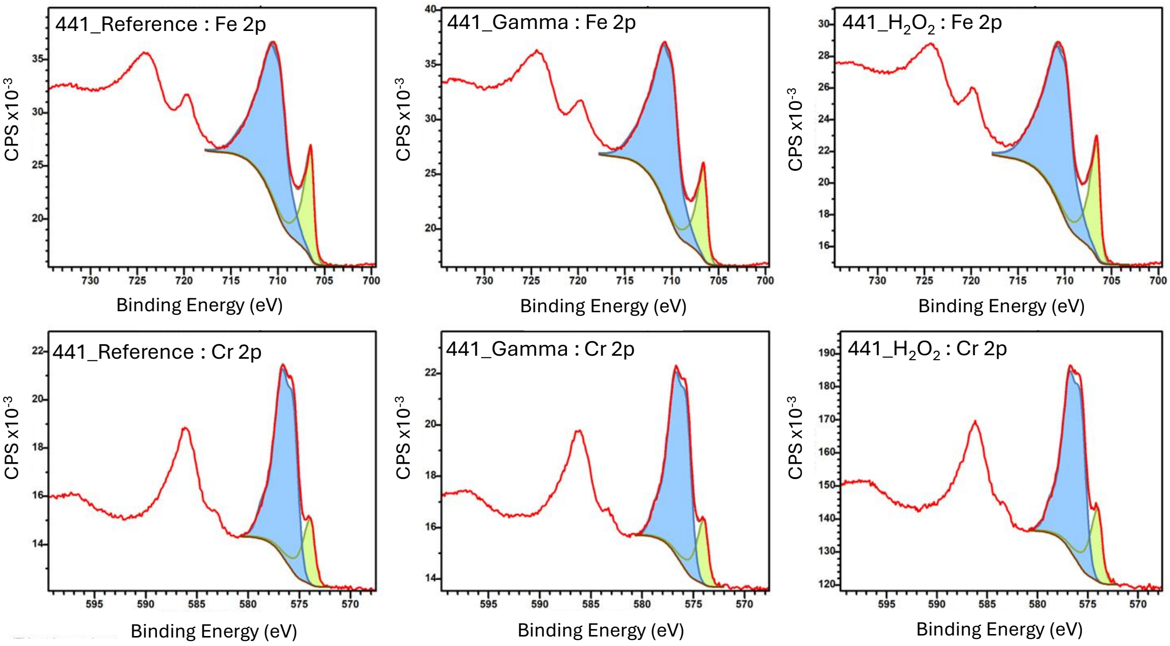

Figure 24: High resolution XPS spectra collected for the AISI 441 alloy samples: as-received (left), irradiated up to 2.2 MGy in water (centre) and submersed for 28 days in a 1 mM solution of H_2O_2 (right). Upper row: fitting of the 2p peaks for Iron in its metallic state (green) and in the form of oxides (blue). Lower row: fitting of the 2p peaks for Cr in its metallic state (green) and in the form of oxide and hydroxide (blue).

The XPS spectra of Inconel 718 samples, shown in **Figure 25** and **Figure 26**, present a slight difference between reference and both irradiated and H_2O_2-treated samples, both similar to each other.

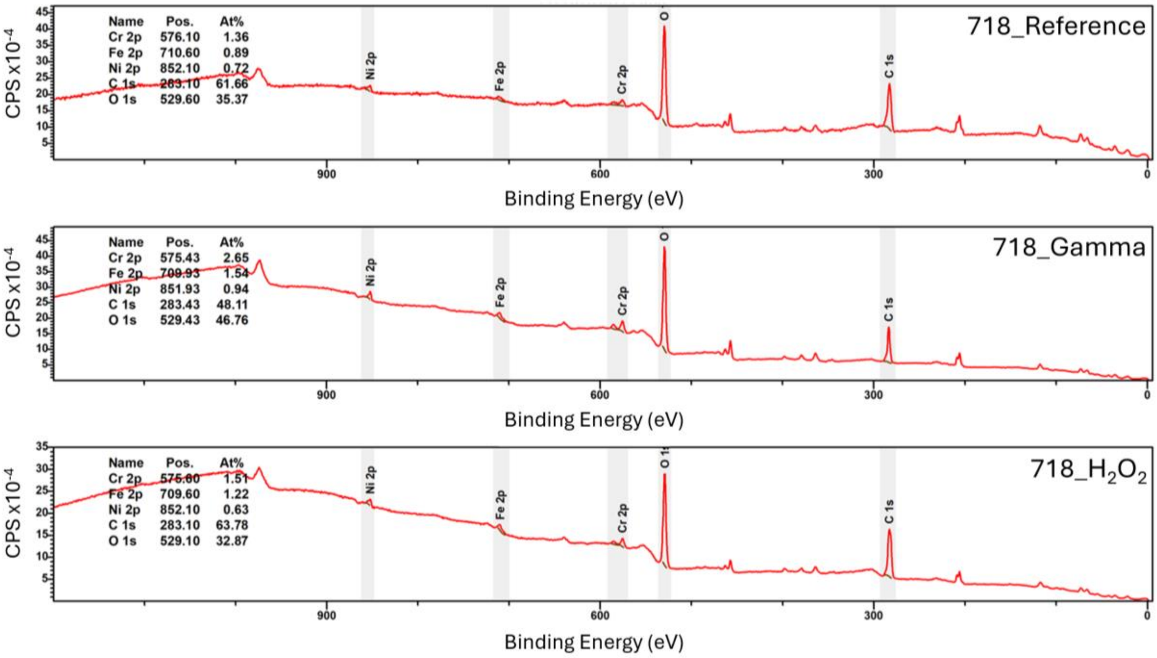

Figure 25: XPS wide spectra collected for the Inconel 718 alloy samples: as-received (top), irradiated up to 2.2 MGy in water (centre) and submersed for 28 days in a 1 mM solution of H_2O_2 (bottom).

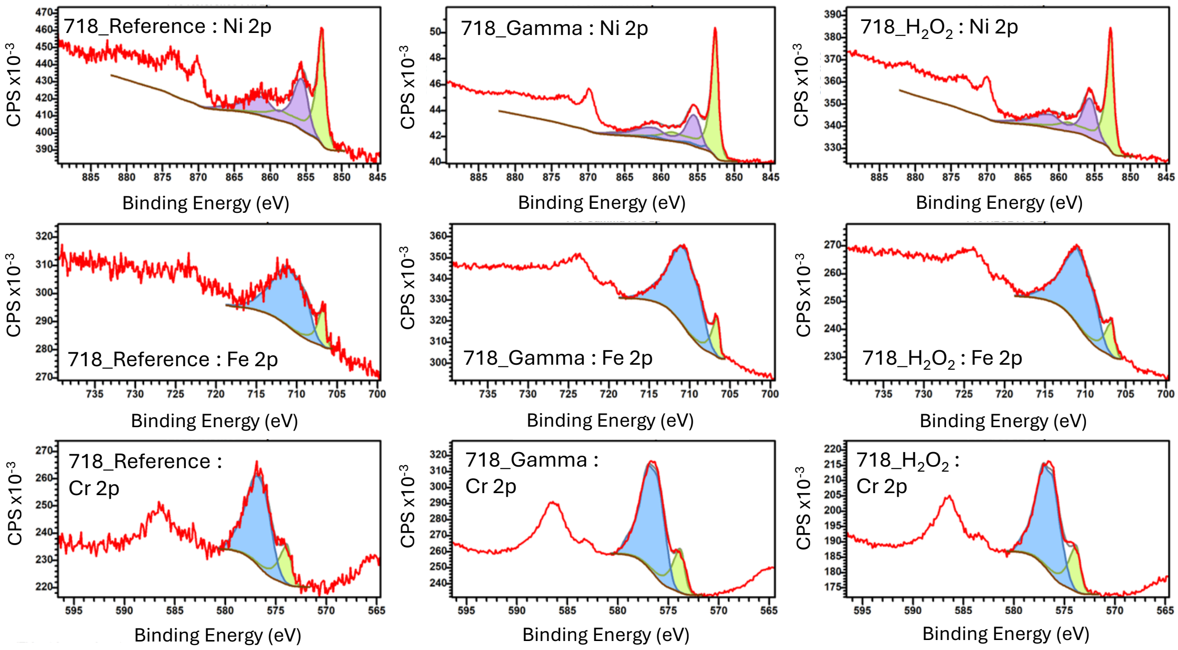

Figure 26: High-resolution XPS spectra collected for the Inconel 718 alloy samples: as-received (left), irradiated up to 2.2 MGy in water (centre) and submersed for 28 days in a 1 mM solution of H_2O_2 (right). Upper row: fitting of the 2p peaks for Ni in its metallic state (green) and in the form of hydroxide (purple). Middle row: fitting of the 2p peaks for Fe in its metallic

state (green) and in the form of hematite (blue). Lower row: fitting of the 2p peaks for Cr in its metallic state (green) and in the form of nickel chromite spinel ($NiCr_2O_4$, blue).

The high-resolution XPS spectra of Inconel 718 samples, shown in **Figure 26**, highlights how the oxidation state of Cr seems to be unchanged over all the samples. Iron seems to be slightly more oxidised for both the irradiated and the H_2O_2-submerged samples, which respectively present 3 and 2.5% more hematite. Nickel seems to be the most affected, with around 51% of metallic Ni, 1% of NiO and 48% of $NiOH_2$ on the reference sample, turning into 59.8% metallic Ni, 4.9% NiO and 35.3% of $NiOH_2$ on the irradiated sample. On the sample that was submerged in H_2O_2, metallic Ni accounts for 57%, and $NiOH_2$ for 43%. The large overlapping of NiO and $NiOH_2$ peaks makes their deconvolution a challenging endeavour. Therefore, the complete absence of NiO from the H_2O_2-treated sample cannot be completely trusted. Overall, it appears that both the irradiation and the submersion in H_2O_2 increased the metallic Ni and the oxidised Fe in the form of hematite. However, strong signals for metallic Ni, Fe and Cr are identified in all the samples, being an indication that the scales are well below 10 nm and that the difference between reference and Irradiated/H_2O_2-treated samples should not exceed 1 nm.

The XPS spectra of Inconel X-750 samples, presented in **Figure 27** andFigure **26**, also exhibit a slight difference between reference and both irradiated and H_2O_2-treated samples. Again, both are quite similar to each other.

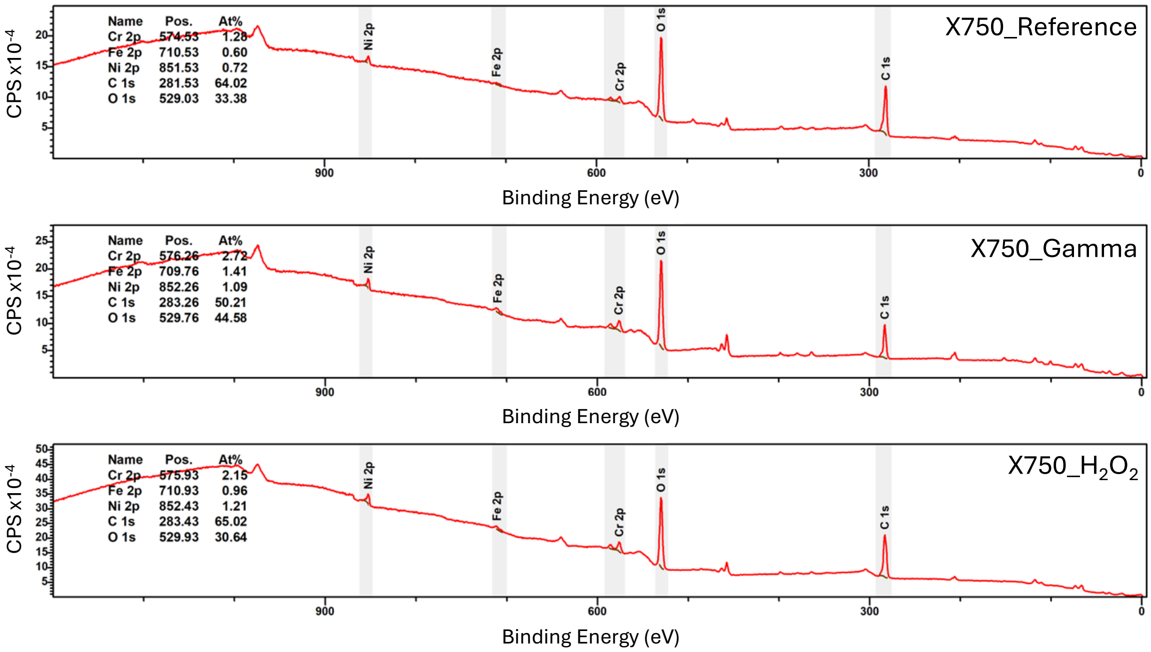

Figure 27: XPS wide spectra collected for the Inconel *X-750* alloy samples: as-received (top), irradiated up to 2.2 MGy in water (centre) and submersed for 28 days in a 1 mM solution of H_2O_2 (bottom).

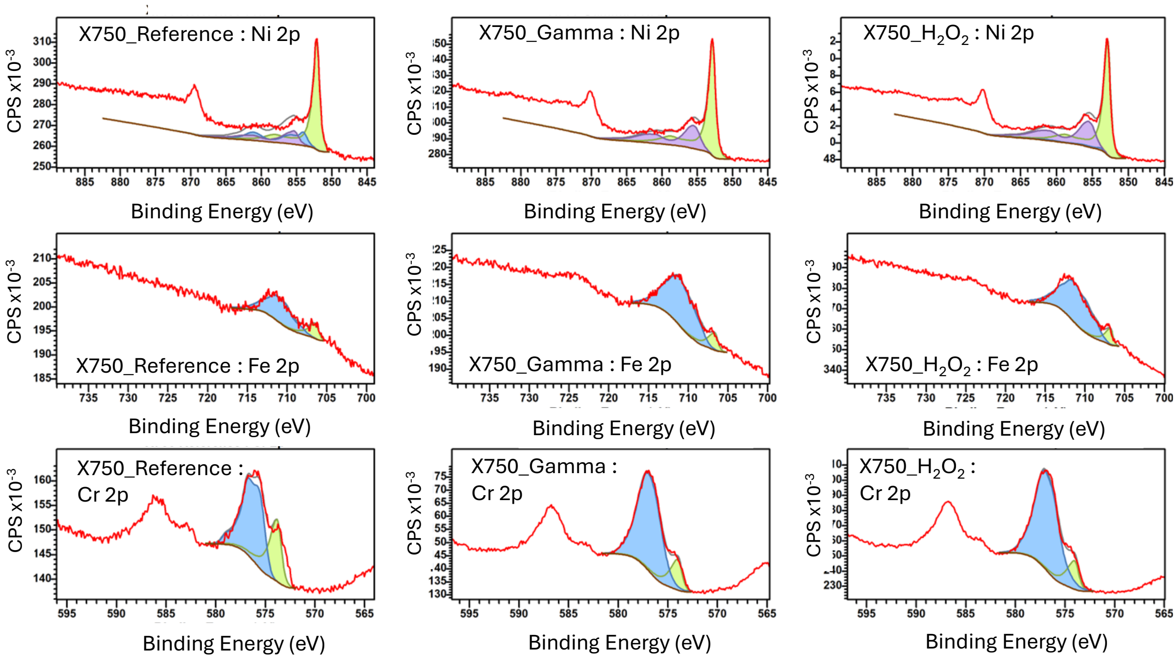

Figure 28: Detailed XPS spectra collected for the Inconel X-750 alloy samples: as-received (left), irradiated up to 2.2 MGy in water (centre) and submersed for 28 days in a 1 mM solution of H_2O_2 (right). Upper row: fitting of the 2p peaks for Ni in its metallic state (green) and in the form of oxide (blue), and hydroxide (purple). Middle row: fitting of the 2p peaks for Fe in its metallic state (green) and in the form of oxide (blue). Lower row: fitting of the 2p peaks for Cr in its metallic state (green) and in the form of oxide and hydroxide (blue).

From the high-resolution XPS spectra of the Inconel X750 alloy samples presented in **Figure 28** and their deconvolutions, the percentage of metallic Ni is almost identical for the reference and the sample exposed to H_2O_2, whereas it is 6 % higher for the irradiated sample. The percentages of Nickel oxide and hydroxide are instead varying between reference and irradiated/H_2O_2 samples, but their quantification is difficult, as explained for Inconel 718. Higher relative percentages of both Fe (10%) and Cr (16-17%) are in their oxidised state in both the irradiated/H_2O_2 samples with respect to the as-received one. As for the previous materials, X-750 samples also exhibit strong metallic signals, indicating an overall oxide thickness well below 10 nm and differences between reference and treated samples reasonably below 1 nm.

The XPS spectra of Zircalloy-2 samples, presented in **Figure 29** and **Figure 30**, exhibit virtually no difference between reference and both irradiated and H_2O_2-treated samples. Focusing on the high-resolution spectra of Figure 30, the relative percentage of ZrO_2 is slightly above 95% for all the samples. A weak signal, just above 4%, is obtained for metallic Zr from the deconvolution of the spectra. These data suggest a thicker scale, probably around 10 nm, for all the studied samples.

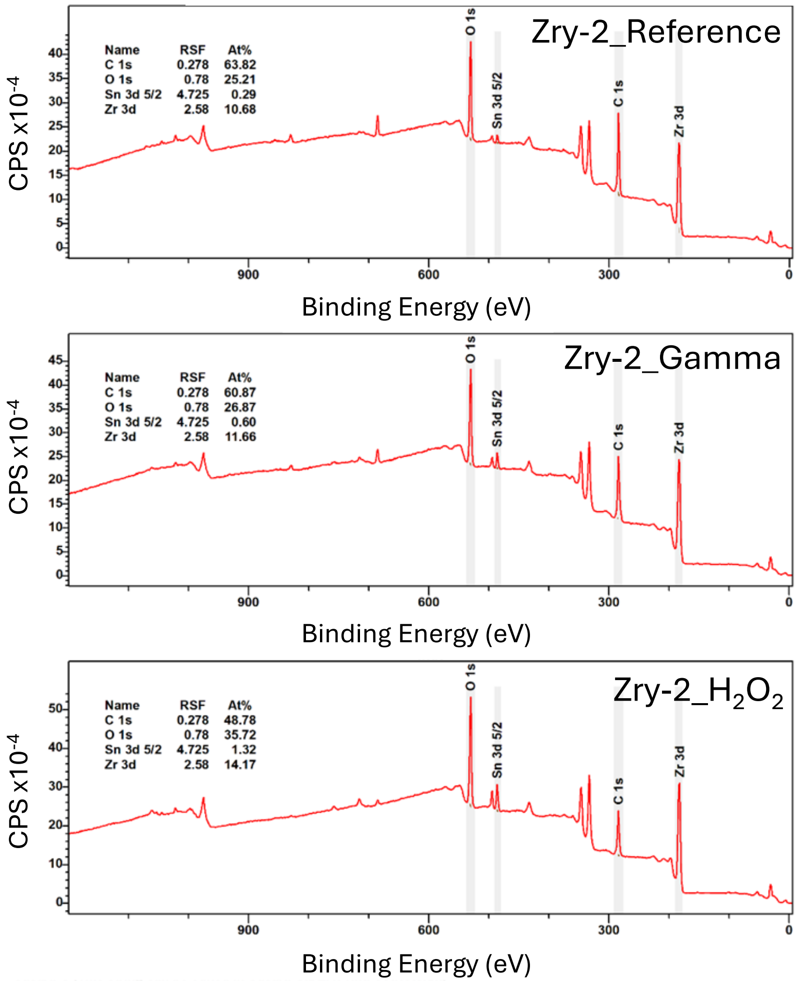

Figure 29: XPS wide spectra collected for the Inconel Zry-2 alloy samples: as-received (top), irradiated up to 2.2 MGy in water (centre) and submersed for 28 days in a 1 mM solution of H_2O_2 (bottom).

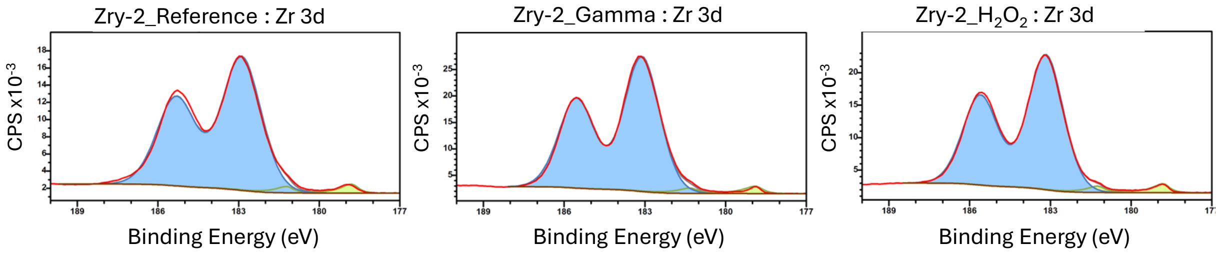

Figure 30: Detailed XPS spectra collected for the Zircalloy-2 samples: as-received (left), irradiated up to 2.2 MGy in water (centre) and submersed for 28 days in a 1 mM solution of H_2O_2 (right). The fitting shown is for the 3d peaks for Zr in its metallic state (green) and in the form of oxide (blue).

To resume, XPS analysis pointed out only minor composition differences between as-received/irradiated and H_2O_2-treated samples. These minor differences are related to the relative metal/oxides/hydroxides compositions of the surface. However, the peaks associated with the metallic state are always visible, being a reliable indicator of thin (i.e., a few nanometer-thick) oxide layers on the surface of the investigated alloys both before and after irradiation or submersion in 1 mM H_2O_2 solution. XPS Investigations are therefore consistent with SEM micrographs.

5.4. Electrochemical Studies

Given the physical characteristics of the oxide layer of the tested samples and the necessity to quantify it with a fast and scalable method, the samples have been investigated employing electrochemical impedance spectroscopy, as explained in detail in **3.2.5**. The measurements performed are presented in **5.4.1**.

To open the path to a better understanding of the effect of gamma irradiation on the investigated materials, linear sweep voltammetry of the samples has been performed in different atmospheres, electrolytic solutions and under irradiation as well. Furthermore, potentiostatic amperometry under intermittent irradiation has also been performed. The preliminary observations are disclosed in **5.4.2** and **5.4.3**, respectively.

5.4.1. Investigation of Oxide Scale Growth

The EIS investigations carried out on the four alloys in as-received, after irradiation (2.2 MGy) and submerged in H_2O_2 (1 mM, 28 days) conditions are reported in the form of both Bode and Nyquist plots. The results for AISI 441, Inconel 718, Inconel X-750 and Zircalloy-2, presented respectively in **Figure 31**, **Figure 32**, **Figure 33**, **Figure 34** and **Table 3** will be discussed together after the figures.

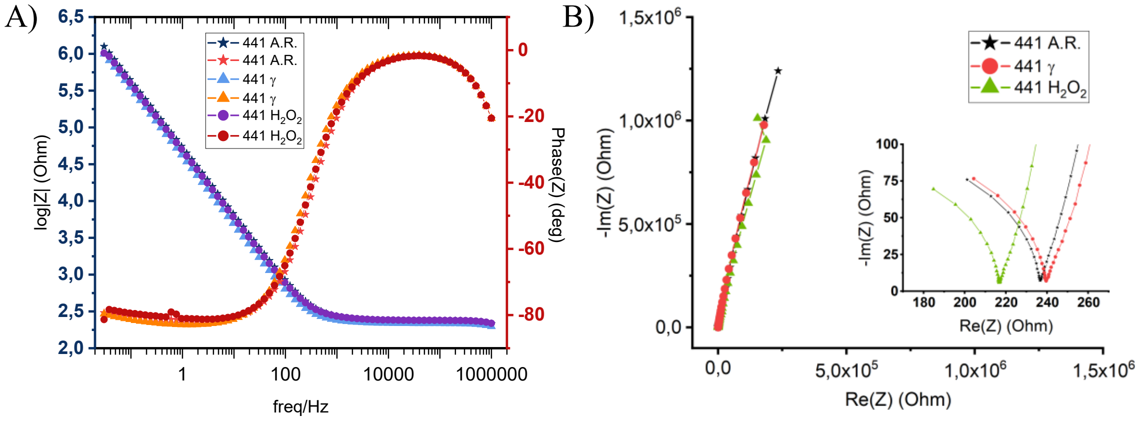

Figure 31: A) Bode and B) Nyquist diagrams of the as-received (A.R.), irradiated (γ, 2.2 MGy) and submersed in H_2O_2 solution (1 mM, 28 days) samples of AISI 441 alloy. In the inset of the Nyquist plot, a zoom-in of the graph, with the first points collected during the EIS measurement.

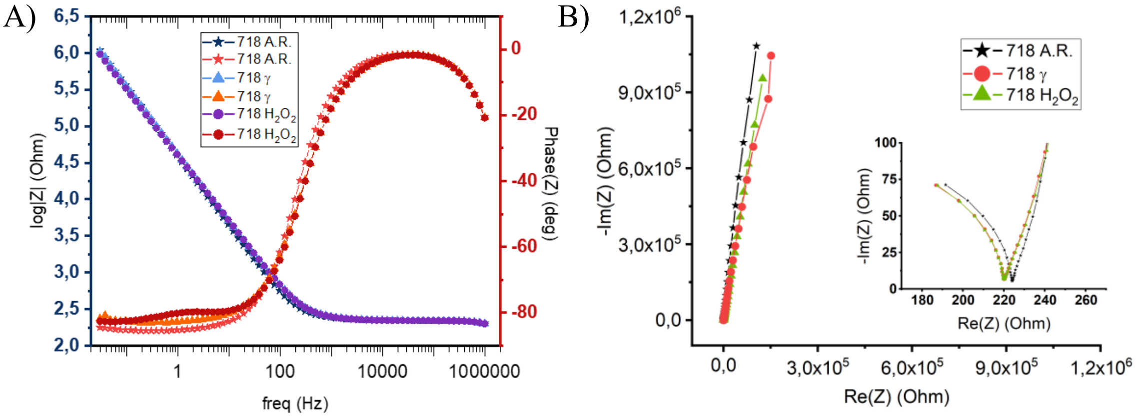

Figure 32: A) Bode and B) Nyquist diagrams of the as-received (A.R.), irradiated (γ, 2.2 MGy) and submersed in H_2O_2 solution (1 mM, 28 days) samples of Inconel 718 alloy. In the inset of the Nyquist plot, a zoom-in of the graph, with the first points collected during the EIS measurement.

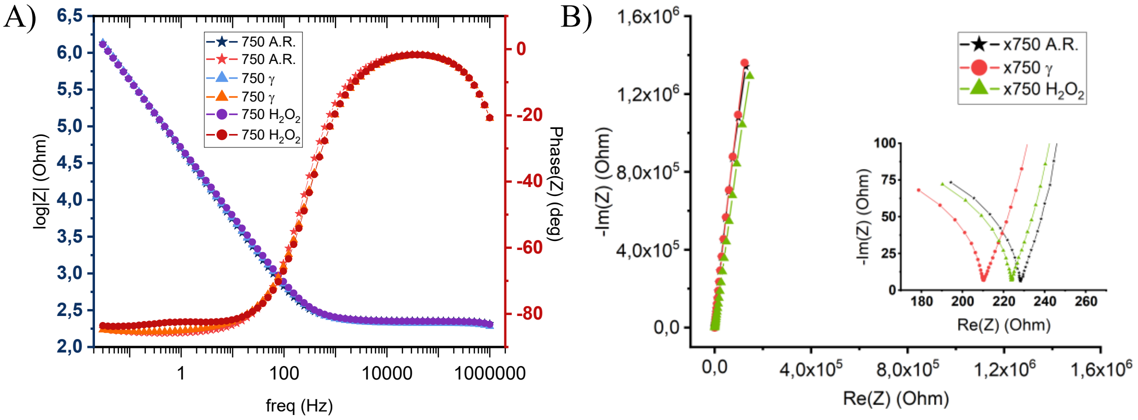

Figure 33: A) Bode and B) Nyquist diagrams of the as-received (A.R.), irradiated (γ, 2.2 MGy) and submersed in H_2O_2 solution (1 mM, 28 days) samples of Inconel X-750 alloy. In the inset of the Nyquist plot, a zoom-in of the graph, with the first points collected during the EIS measurement.

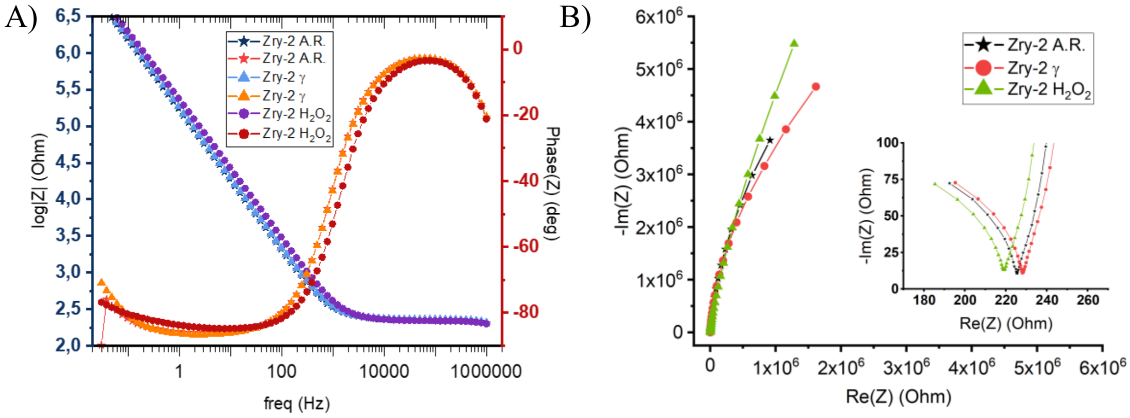

Figure 34: A) Bode and B) Nyquist diagrams of the as-received (A.R.), irradiated (γ, 2.2 MGy) and submersed in H_2O_2 solution (1 mM, 28 days) samples of Zircalloy-2. In the inset of the Nyquist plot, a zoom-in of the graph, with the first points collected during the EIS measurement.

According to the presented data, all the samples are characterised by an almost exclusively capacitive behaviour, which can be easily recognised by its distinctive features in the Bode plot. In fact, the impedance does not reach any plateau at low frequencies for any of the samples. Simultaneously, the phase is rather stable at almost 90 °. Also, the Nyquist plots confirm this, presenting a shape resembling that of a pure capacitor. All the samples are missing what would graphically look like a semicircle and would be associated with the charge transfer resistance at the electrode surface. What may look like a partial semicircle at the highest frequencies (shown in the inlet of **Figure 31, Figure 32, Figure 33** and **Figure 34**) is actually reproducible for all the samples and could be explained by an artefact induced by the instrument itself. Therefore, the calculation of the surface oxide thickness, illustrated in **3.2.5.1** and presented in **Table 3**, is based on the impedance measured at 15.652 kHz, which is the first frequency at which it is possible to gather pieces of information from the samples.Surface Oxide Thickness Calculation from EIS Data

Table 3: Surface oxide estimation, in nm, based on the EIS investigation and the method explained in detail in 3.2.5.1.

	A.R. (nm)	**γ-irradiated (nm)**	**Submerged in H_2O_2 (nm)**
AISI 441	4.6	3.6	4.4
Inconel 718	2.7	3.6	3.7
Inconel X-750	3.3	3.9	3.77
Zircalloy-2	14.5	15.0	20.1

The surface oxide estimations, calculated from impedance data collected through EIS, seem to be in reasonable agreement with the observation made from the XPS spectra. AISI 441, and Inconel alloys are all characterised by very thin (i.e., a few nanometer-thick) oxide layers, with sub-nanometer differences between samples matching remarkably well the XPS data, especially for both nickel-based alloys. As suggested by the analysis of the XPS spectra for Zircalloy-2 samples, the calculated surface oxides are thicker than for the other materials. However, while the ~15 nm thickness of as-received and irradiated Zry-2 samples could be overestimated, but still matches the minimal relative differences between samples, the thickness of the sample submerged in H_2O_2 (20 nm) seems too far from XPS data. Such a discrepancy could be explained by the simplification made for the oxide composition, affecting the dielectric constant. Moreover, the insulating properties of ZrO_2 made XPS measurements more difficult and could have affected EIS measurements as well. Lastly, the as-received surface condition of the samples may have introduced bias not dependent on either irradiation or the prolonged contact with H_2O_2.

5.4.2. Electrochemical Response Under Irradiation

To investigate whether the electrochemical response of the alloys is influenced by gamma radiation, linear sweep voltammetry has been performed for both ground AISI 441 and Zircalloy-2 samples. The alloys were chosen since being the two with the most different effects on H_2O_2 accumulation under irradiation. Since H_2O_2 could potentially take part to both oxidative and reducing processes, both anodic and cathodic LSV have been conducted. Two different atmospheres (air and Ar) and electrolytic solutions (1 $\%^{wt}$ $NaSO_4$ and 1 $\%^{wt}$ $NaSO_4$ + 0.1 mM of H_2O_2) were used. The intent of using an inert atmosphere is to investigate the contribution of reactions involving oxygen. Moreover, removing oxygen, the yield for radiolytically produced H_2O_2 is strongly reduced, O_2 being a precursor for radiolytically produced H_2O_2. The 0.1 mM hydrogen peroxide concentration was chosen since similar to what the solutions would naturally achieve under irradiation for similar time extents. The following results are preliminary and therefore not exhaustive or fully understood yet. The anodic LSV for AISI 441 samples are shown in **Figure 35**.

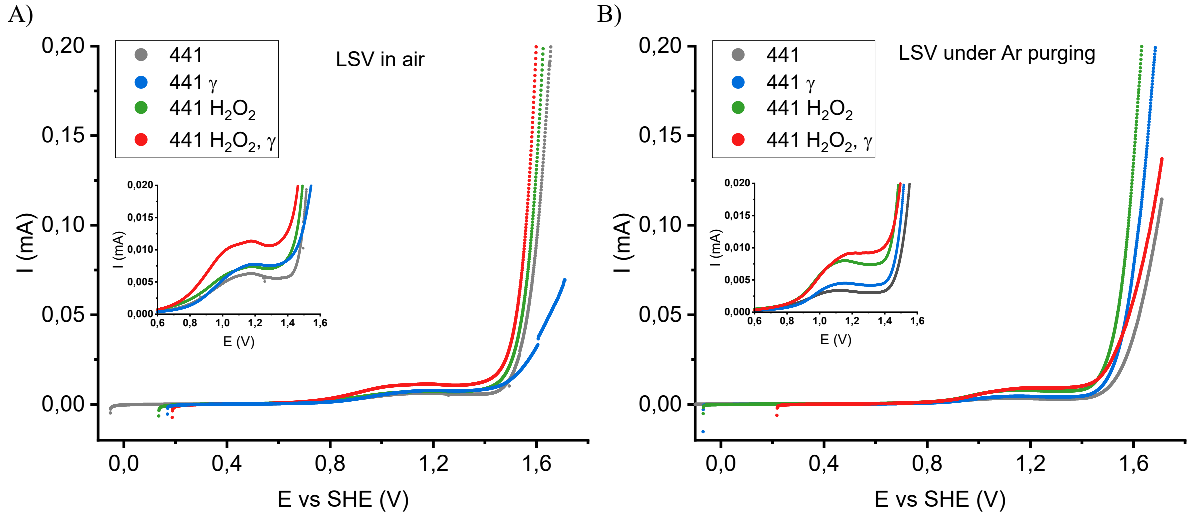

Figure 35: A) Anodic LSV of ground AISI 441 samples in air and B) under Ar atmosphere. The measurements were performed starting from a potential 0.2 V lower than the OCP, toward higher potentials. The samples marked as "γ" have been investigated while under irradiation. The samples marked as "H_2O_2" had 0.1 mM added to the electrolyte.

As visible in **Figure 35**, in air, all the AISI 441 samples present an increase in current starting from around 0.6 V, peaking at 1.1 V and then quickly increasing due to the evolution of oxygen. The addition of H_2O_2 only marginally increases the current, while the irradiation with gamma induces a stronger current increase if H_2O_2 was added to the electrolyte. This may be explained by the beginning of a transpassive behaviour, forcing the oxidation of Cr, assisted by H_2O_2 and radiolytically produced •OH in the vicinity of the WE. Under Argon atmosphere, the response of the samples is largely unaffected. Only the current recorded for the LSV with the addition of H_2O_2 seems higher and almost the same as under irradiation.

The cathodic LSV performed on AISI 441 samples are shown in **Figure 37**.

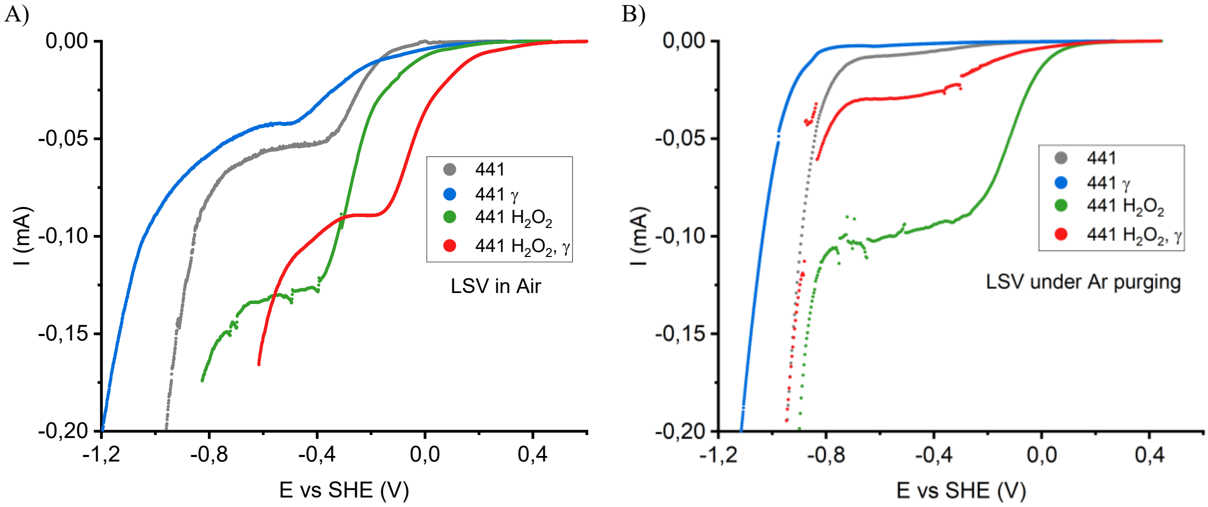

Figure 36: A) Cathodic LSV of ground AISI 441 samples in air and B) under Ar atmosphere. The measurements were performed starting from a potential 0.2 V higher than the OCP, toward

lower potentials. The samples marked as “γ” have been investigated while under irradiation. The samples marked as “H_2O_2” had 0.1 mM added to the electrolyte.

Comparing the cathodic LSV of AISI 441 in air and under Ar (**Figure 37 A** and **B**), it is evident at first glance how oxygen availability makes a large difference. In both atmospheres, γ irradiation (blue lines) seems to delay or hinder reactions from taking place if no H_2O_2 is present beforehand (red lines). However, it is arguable that the current increase observed without adding H_2O_2 (grey and blue lines), from around -0.3 V is related to the availability of oxygen, with the reduction of oxygen being the strongest candidate.

Under argon (**Figure 36 B**), In the presence of a 0.1 mM concentration of H_2O_2 (green line), the current is rather high (in relation to the measurement without H_2O_2, grey line), but it gets lower when γ-radiation is simultaneously applied (red line). However, onset potentials and shapes are similar, suggesting that the reaction(s) taking place could reasonably be H_2O_2 reduction, eventually inhibited by γ-radiation. In air (**Figure 36 A**), the presence of 0.1 mM H_2O_2 (green line) increases the current, maintaining similar onset potentials and shape of the curve for the bare electrolyte without irradiation (grey line). Under irradiation (blue line), the beginning of the current increase takes place at a potential 0.15 V lower, indicating a possible catalytic effect involving species in solution. Even so, the current is not as high as without γ-radiation (grey line), reaching a plateau before the evolution of hydrogen, which also happens at a lower (0.1 V) potential. Overall, the irradiation of AISI 441 mildly supports oxidative reactions while markedly hinders reducing reactions on the surface of the alloy. Most importantly, the Hydrogen Evolution Reaction (HER) is distinctly delayed during the irradiation of AISI 441 in bare electrolytic solution, regardless of the presence of oxygen. In the presence of H_2O_2, the HER seems to be catalysed on the surface of AISI 441 if oxygen is also present, and slightly delayed in inert atmosphere.

The anodic LSV performed on Zircalloy-2 samples, shown in **Figure 37,** exhibit interesting characteristics. In air (**Figure 37 A**), for both bare sodium sulfate solution (grey line) and with hydrogen peroxide (green line), the irradiation of the sample increases the current (blue and red line). However, they reach the same currents under irradiation, possibly indicating a diffusion-controlled condition independent from the concentration of H_2O_2 or other products of radiolysis. Interestingly, without radiation, the addition of hydrogen peroxide to the electrolyte (green line) anticipates the current increase with respect to the standard electrolyte (grey line), capping the maximum current at a lower intensity as well (green line). A possible explanation could be the ease of some oxidative, H_2O_2-assisted reactions (e.g., passivation) on the sample that, in turn, made the surface scale less reactive. This further hinders the diffusion-controlled phenomena, causing a lower quasi-stable current observed even at higher voltages.

In argon atmosphere (**Figure 37 B**), currents are at least one order of magnitude lower than in air (**Figure 37 A**). Contrary to air, irradiation of the sample in bare Na_2SO_4 drastically reduces the current, without altering the onset (blue line). When H_2O_2 is added to the electrolyte, the onset is anticipated, and the maximum current is lower (green line). If the hypothesis made before for the sample in air were true, then we could say that the oxidative reaction involving the surface oxide is primarily H_2O_2-mediated, as it takes place also in an oxygen-free atmosphere. The irradiation of the sample in contact with the 0.1 mM H_2O_2 electrolyte anticipates and enlarges the current increase (red line).

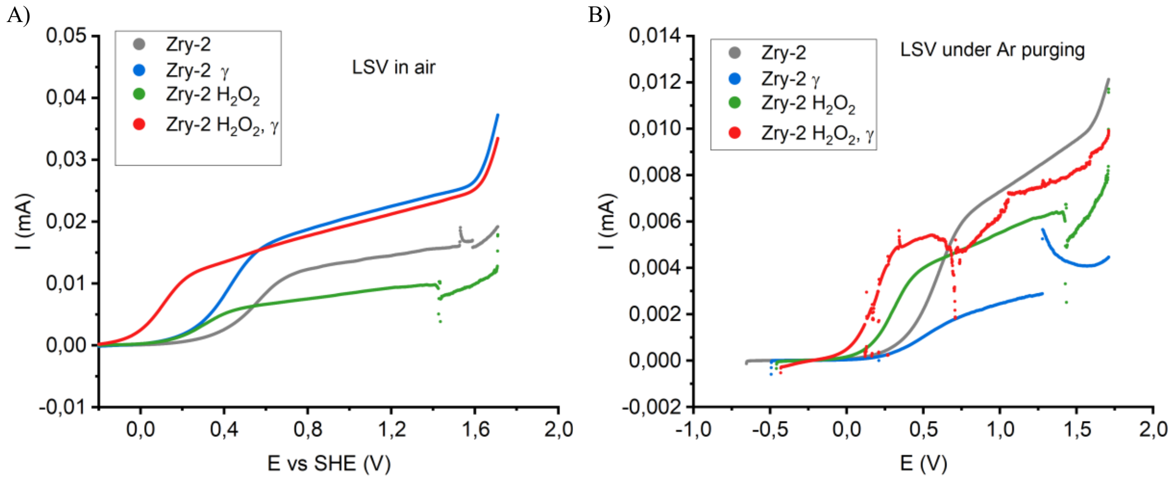

Figure 37: A) Anodic LSV of as-received Zircalloy-2 samples in air and B) under Ar atmosphere. The measurements were performed starting from a potential 0.2 V lower than the OCP, toward higher potentials. The samples marked as "γ" have been investigated while under irradiation. The samples marked as "H_2O_2" had 0.1 mM added to the electrolyte.

During cathodic polarisation, Zircalloy samples show extremely low reactivity, compared to AISI 441, as visible in **Figure 38**.

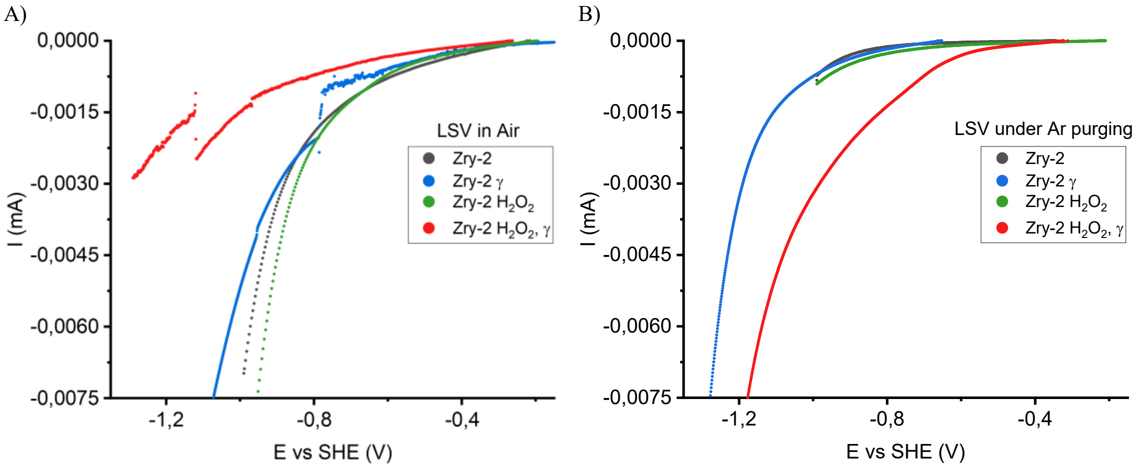

Figure 38: A) Cathodic LSV of as-received Zircalloy-2 samples in air and B) under Ar atmosphere (right). The measurements were performed starting from a potential 0.2 V higher than the OCP, toward lower potentials. The samples marked as "γ" have been investigated while under irradiation. The samples marked as "H_2O_2" had 0.1 mM added to the electrolyte.

Both in air and in argon atmosphere, Zircalloy-2 samples exhibit quite a homogeneous behaviour. In fact, the irradiation of the alloy in bare sodium sulfate solution (blue line) and the addition of hydrogen peroxide up to 0.1 mM (green line) do not seem to affect the recorded current. Only the onset of the Hydrogen Evolution Reaction (HER) seems to happen. When the irradiation takes place on the samples submerged in the H_2O_2-spiked electrolyte, a marked difference is recorded instead. In the air, the onset of the HER happens at the same potential, but the current grows more slowly (red line). Unfortunately, it is impossible to comment further on the HER since the measurement has been interrupted due to external factors. Conversely, the irradiation of Zircalloy-2 in the same electrolyte but in Argon anticipates the onset of HER, with the current increasing at a faster pace. The electrochemical behaviour of Zircalloy-2 seems to be heavily affected by oxygen, with gamma irradiation promoting oxidation over reduction on the surface of the alloy in air. In argon, both oxidation and reduction seem to be enhanced by γ-irradiation. However, new measurements are required, given the noise and disturbances recorded for different measurements and the peculiar characteristics.

Comparing the two materials more comprehensively, we can point out a larger reactivity of AISI 441 than Zircalloy-2 in reduction and more complex but also less different behaviours in oxidation. These general observations, correlated with the lower concentration of radiolytically-produced H_2O_2 accumulated by AISI 441 samples with respect to Zry-2 (**Figure 15**), may be an indication that the γ-irradiation promoted reduction reactions on the surface of the samples.

5.4.3. Potentiostatic Amperometry Under Intermittent Irradiation

Potentiostatic amperometric measurements at the OCP of AISI 441 and Zircalloy-2 samples have been performed while intermittently irradiating them by lowering and raising the irradiation chamber, where the EC cell was accommodated, inside the Gammacell-220 source. The experiments have been performed in 1 %^{wt} Na_2SO_4 (70 mM) with and without the addition of H_2O_2 up to 20 mM, as presented in **Figure 39**. The 20 mM concentration of hydrogen peroxide, being c.a 100 times higher than in the previous irradiation experiments, aims at exacerbating eventual reactions involving such species. On the other side, the intermittent irradiation of bare electrolytic solution is expected to produce H_2O_2 concentration between 60 to 80 μM, roughly half of the concentration achieved in 4 hours of irradiation (as shown in the inset of **Figure 11**).

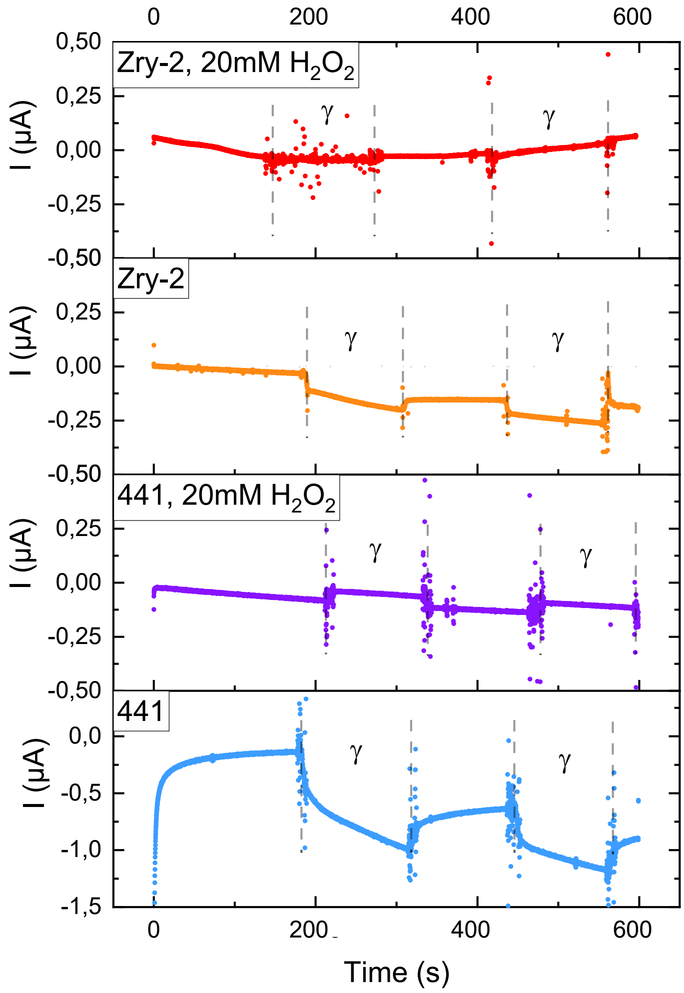

Figure 39: Potentiostatic amperometry measurements of as-received Zircalloy-2 (top two) and AISI 441 (bottom two) samples at their OCP, under intermittent gamma irradiation. Samples have been investigated in both bare electrolytic solution and with the addition of H_2O_2 up to 20 mM in the same. Note the different scales on the current axes.

As visible in **Figure 39**, the current varies at the same moment γ-radiation reaches the samples, to then come back to values closer to those before irradiation, when this is suspended. Interestingly, both materials exhibit a weaker response to radiation when tested in an electrolytic solution containing 20 mM of H_2O_2. AISI 441 (in purple) starts from a low, negative current (~0.05 µA, due to the shift of the OCP to a potential higher than the one set for the measurement), to adjust itself to a less negative one. Such behaviour indicates a shift of the OCP towards a more negative potential. Such a shift may find explanation in the alteration of the electrolytic solution due to the formation of other radiolytic products besides the pre-existing H_2O_2 and/or a variation of its concentration. In the same conditions, the Zircalloy sample has almost no response to the irradiation (in red), with a barely detectable adjustment to higher currents. Such a variation is a symptom of the OCP shifting toward a more positive potential; therefore, the opposite of AISI 441.

In the Experiments performed with bare sodium sulfate-based electrolyte, both samples (in orange and blue) react more vigorously, and both adjust to more negative currents, as the OCP shifts to a more positive potential. However, AISI 441 OCP is the most affected, with a shift 10 times larger than that of Zircalloy-2. The variation is of roughly 0.1 µA for Zry-2 and more than 1 µA for AISI 441. In general, the amplitude of the response of both materials seem to be in agreement with their effect on the H_2O_2 accumulation under irradiation presented in **5.2**, despite the received dose of the samples being 4 orders of magnitude lower.

5.5. Determination of Ions in Aqueous Phase

Given the known qualitative composition of the studied alloys, ICP-MS analysis was performed on the water solutions in which the coupons had been irradiated. The investigation was performed on the solutions of both as-received and ground samples. The elements whose traces have been found have been collected in **Table 4** with their respective concentrations.

Table 4: Concentration, in ppb, of the elements identified in the solutions where alloy samples were accommodated during irradiation (2.2 MGy). UDL stands for “under detection limit”.

	Ti-48		**Fe-57**		**Ni-60**		**Nb-93**	
	Conc. (ppb)	**SD**	**Conc. (ppb)**	**SD**	**Conc. (ppb)**	**SD**	**Conc. (ppb)**	**SD**
441 A.R.	0,54	1,08	25,74	1,23	UDL		UDL	
718 A.R.	3,05	0,78	5,25	1,63	44,32	0,59	UDL	
x750 A.R.	15,96	1,23	1,33	1,42	60,80	0,78	10,24	0,64
Zry2 A.R	UDL		UDL		0,50	0,03	UDL	
441 ground	0,86	0,66	39,45	0,70	1,33	0,04	UDL	
718 ground	3,76	1,08	4,06	1,14	43,26	0,84	UDL	
x750 ground	26,86	0,95	UDL		78,24	1,75	22,96	0,99
Zry2 ground	0,29	0,70	1,88	0,52	1,17	0,03	UDL	

As visible in **Table 4**, of 12 elements involved in the investigation, only 4 were detected. A fifth one, Al, was also detected with concentrations above 500 ppb for all the samples. Such a high concentration is reasonably due to the dissolution of aluminium from the lining of the septa, with good reason caused by the HNO_3 formed by the irradiation of humid air and therefore excluded from the table. AISI 441, Inconel X-750 and Zircalloy-2 share slightly higher concentrations of the various identified elements in their ground sample than in the as-received ones. It can be reasonably explained by the larger surface in contact with the solution and the thinner/less protective surface oxide. Interestingly, Inconel 718 does not present the same characteristic, with detected concentrations more homogeneous between A.R. and ground sample solutions. AISI 441 samples are characterised by concentrations of Fe (which readily react with hydrogen peroxide) higher than the other samples. Inconel 718 presents the second highest concentration of Fe after AISI 441, and the second highest concentration of Ni after Inconel X-750.

Since the ICP-MS analysis presented above has been performed on the solutions collected from the vials used for irradiation, after adequate dilution with nitric acid, eventual precipitates or materials adsorbed on the surfaces of the containers have been arguably lost. This aspect could be of great importance, especially for Fe^{2+}, known to react promptly with H_2O_2 and able to form insoluble hydroxides and oxides. However, it is important to point out the correlation between the higher Fe concentration in solution and the lower H_2O_2 accumulation under irradiation for the same alloys. Concurrently, Zircalloy-2 is the material with the lowest elemental traces in solution and the one with the highest H_2O_2 concentration after irradiation. Nonetheless, it is debatable whether or not Ni plays a role. Inconel X-750 samples have higher (60 to 80 ppb) concentration of Ni, while Inconel 718 presents less Fe than AISI 441, but twice as much as Inconel X-750 and the two materials produced variable hydrogen peroxide concentrations under irradiation.

6. Conclusions

It has been proved that the choice of septa of sealed glass vials plays a fundamental role in experimental reproducibility and the production of reliable data. It is, in fact, evident that the investigated materials affect the buildup of H_2O_2 in water under gamma irradiation. In particular, it was demonstrated that silicone rubber facing the headspace of the vials strongly reduces H_2O_2 long-term concentration at high doses (above 14.8 kGy). The phenomenon is arguably due to the depletion of O_2 in the vials through reactions with the carbon-centred radicals formed in the polymer of the septa by γ-radiation. The outcome of this investigation highlights the importance of using the right septum material when irradiating aqueous solutions to doses higher than 10 kGy, and laid the foundations for the other investigations presented in this thesis.

Gamma irradiation of alloys (AISI 441, Inconel 718 and X-750, and Zircalloy-2) submersed in water proved that H_2O_2 accumulation due to radiolysis is affected by the elemental formulation of the alloys themselves. Tests with different alloys' surface finishing (e.g., ground surface) provided similar results, consolidating the outlined trend. H_2O_2 stability in the presence of the same alloys was proved to be only minimally different for the various alloy formulations. Therefore, the alteration of the H_2O_2 accumulation was proved to be triggered by gamma irradiation, with AISI 441 being the one affecting it the most negatively and Zircalloy-2 the only one with a neutral or even positive effect on it.

Gamma irradiation of AISI 316L alloy samples in water, previously pre-oxidised to achieve different surface oxide thicknesses, possibly revealed a correlation between the morphological (e.g., thickness, roughness, porosity) and chemical properties of the surface oxide and the concentration of H_2O_2 accumulated in the solution. However, it was impossible to completely restore the concentration up to the levels reached by irradiation of bare water.

The surface of the samples was investigated by SEM and XPS analysis, indicating the presence of a few-nanometer-thick oxide layer both before and after irradiation. Alterations of the oxide layer due to exposure to radiolysis products, γ-radiation, and chemically added H_2O_2 within the tested conditions were minimal and uncertain.

EIS investigation of the alloys corroborated the SEM and XPS results, proving to be a versatile and non-destructive analysis able to provide numerical estimations of the surface oxide thickness, even for such thin oxides. Only the EIS-calculated Zircalloy-2 oxide thickness deviates from XPS estimations. Such a matter is arguably due to the simplifications used for the calculations and the challenges of analysing such a low-conductive sample.

ICP-MS analysis of the solutions hosting the alloys under irradiation revealed minimal traces (i.e., from a few ppb to tens of ppb) of some elements, arguably released by the alloys themselves. In particular, the solutions in which AISI 441 samples were submerged during irradiation present a higher concentration of Fe concerning the others.

Overall, the diminished H_2O_2 concentration in irradiated water in contact with the alloys, especially AISI 441, cannot be justified by oxidative processes involving the growth of a thicker oxide scale. On the other hand, it could be correlated to higher elemental concentrations found in the solutions, especially Iron, as proved for AISI 441.

Further preliminary electrochemical studies, namely linear sweep voltammetry and potentiostatic amperometry, may indicate possible correlations between the enhanced electrochemical response of AISI 441 under irradiation and its influence on H_2O_2 accumulation in solution.

7. Future Work

In the near future, further electrochemical studies will be performed to improve the quality of existing data and corroborate the considered correlation. In particular, LSV measurements will be repeated, aiming at expanding the range of potential voltages investigated and collecting currents possibly unaffected by noise and biases. CA under intermittent irradiation will be performed again, striving for the choice of better OCP-representing polarisation voltages and the modulation of the dose-rate, using lead shields of different thicknesses.

The Gamma irradiation of alloys with water in unsealed vials will be repeated to confirm the observed trends. AISI 316L and other alloys, such as AISI 441, will be pre-oxidised through a thermal treatment and subsequently irradiated while submerged in water to explore the reproducibility of the trend already observed for AISI 316L. Subsequently, XPS and SEM investigation of such samples will be carried out, to determine morphology and composition of the oxide scale.

ICP-MS investigations will be expanded, aiming at dissolving and collecting eventual precipitates in the irradiated solution, allowing for their identification and elemental quantification.

In September 2024, a γ-irradiation campaign at high temperature and pressure (to mimic actual reactor conditions) was performed in collaboration with the Dalton Nuclear Facility of the University of Manchester, in the UK. Samples' characterisation has started already. However, some of the planned experiments needed for a comparison have been postponed. The intention is to complete the experimental campaign and to disclose the results in a scientific article.

The exploitation of the constructed electrochemical setup for the investigation and validation of pH titration under γ-irradiation is also under consideration.

Acknowledgements

I want to express my gratitude to the Swedish Centre for Nuclear Technology, SKC, for funding the project “Impact of Radiation Chemistry on Surface Processes in LWRs”, of which the work presented in this thesis is part.

Thank you to my supervisor, Professor Mats Jonsson, for finding the time to discuss science with me despite the distance and his busy schedule. I truly appreciate your time and kindness.

Thank you to my co-supervisor, Professor Christian Ekberg, for his bits of advice, for welcoming me into his group and introducing me to proper midsummer celebrations.

Thank you, Professor Teodora Retegan Vollmer, for your advice and for being there to listen.

A special thank you to Dr. Alberto Visibile for introducing me to the wonders (and horrors) of electrochemistry and never letting me down when in need, at work and in life.

My sincere appreciation to Professor Nina Kann and Professor Lars Öhrström for the dedication they invest in their educational roles.

Thank you to my colleagues -both past and present- and friends in the Nuclear Chemistry and Industrial Material recycling group at Chalmers, you make the work environment better.

Mamma, Papà, Marco - despite the distance, I feel you close and I can only be grateful for the caring affection that you have always surrounded me with.

My love and gratitude to my wonderful wife, Camilla, for supporting me in every circumstance, celebrating my achievements even when I couldn’t see them myself, and infusing me with confidence when I struggled. You are my source of strength.

References

[1] World Nuclear Association, “World Energy Needs and Nuclear Power.” Accessed: Mar. 31, 2025. [Online]. Available: https://world-nuclear.org/information-library/current-and-future-generation/world-energy-needs-and-nuclear-power

[2] *World Energy Outlook 2023*. OECD, 2023. doi: 10.1787/827374a6-en.

[3] Intergovernmental Panel on Climate Change, “IPCC Sixth Assessment Report,” 2022. [Online]. Available: https://www.ipcc.ch/assessment-report/ar6/

[4] Statista, “Sweden energy mix 2024 | Statista,” www.statista.com. Accessed: Mar. 31, 2025. [Online]. Available: https://www.statista.com/statistics/1013726/share-of-electricity-production-in-sweden-by-source/

[5] SKGS, “The Swedish Industry’s demand for electricity up to 2035,” Jun. 2024. Accessed: Mar. 31, 2025. [Online]. Available: https://skgs.org/english/aktuellt/new-report-the-swedish-industrys-demand-for-electricity-up-to-2030/

[6] Vattenfall press release, “Vattenfall takes the next step for new nuclear power at Ringhals,” Vattenfall website. Accessed: Mar. 31, 2025. [Online]. Available: https://group.vattenfall.com/se/nyheter-och-press/pressmeddelanden/2024/vattenfall-tar-nasta-steg-for-ny-karnkraft-vid-ringhals

[7] IAE, “The Path to a New Era for Nuclear Energy,” Paris, Jan. 2025. Accessed: Mar. 31, 2025. [Online]. Available: https://www.iea.org/reports/the-path-to-a-new-era-for-nuclear-energy

[8] E. English and J. Donovan, “IAEA Data Animation: Nuclear Power Plant Life Extensions Enable Clean Energy Transition.”

[9] Fortum press release, “Owners of Oskarshamn nuclear power plant in Sweden investigate lifetime extension,” Fortum website. Accessed: Mar. 31, 2025. [Online]. Available: https://www.fortum.com/media/2024/09/owners-oskarshamn-nuclear-power-plant-sweden-investigate-lifetime-extension

[10] Vattenfall press release, “Forsmark and Ringhals nuclear power plants aim for 80 years of operation of existing reactors,” Vattenfall website. Accessed: Mar. 31, 2025. [Online]. Available: https://group.vattenfall.com/press-and-media/pressreleases/2024/forsmark-and-ringhals-nuclear-power-plants-aim-for-80-years-of-operation-of-existing-reactors

[11] “PRIS - Reactor status reports - In Operation & Suspended Operation - By Type.” Accessed: Mar. 19, 2025. [Online]. Available: https://pris.iaea.org/pris/worldstatistics/operationalreactorsbytype.aspx

[12] “Power plants: Ringhals - Vattenfall.” Accessed: Mar. 19, 2025. [Online]. Available: https://powerplants.vattenfall.com/ringhals/

[13] “Power plants: Forsmark - Vattenfall.” Accessed: Mar. 19, 2025. [Online]. Available: https://powerplants.vattenfall.com/forsmark/

[14] “Oskarshamn 3 - OKG.” Accessed: Mar. 19, 2025. [Online]. Available: https://www.okg.se/en/oskarshamn-3

[15] K. H. Neeb, “The radiochemistry of nuclear power plants with light water reactors,” *The Radiochemistry of Nuclear Power Plants with Light Water Reactors*, pp. 1–740, 1997, doi: 10.1515/9783110812015.

[16] United States Nuclear Regulatory Commission, “Animated Images of Plants PWR and BWR.” Accessed: Apr. 04, 2025. [Online]. Available: https://www.nrc.gov/reading-rm/basic-ref/students/multimedia/animated-images-plants-pwr-bwr.html

[17] S. Le Caër, “Water Radiolysis: Influence of Oxide Surfaces on H2 Production under Ionizing Radiation,” *Water (Basel)*, vol. 3, no. 1, pp. 235–253, Feb. 2011, doi: 10.3390/w3010235.

[18] A. O. Allen, “Radiation chemistry of aqueous solutions,” *Journal of Physical and Colloid Chemistry*, vol. 52, no. 3, pp. 479–490, 1948, doi: 10.1021/J150459A009/ASSET/J150459A009.FP.PNG_V03.

[19] F. Cattant, “The Underestimated Role of the Oxygen on RCS Components Failures,” 2017. [Online]. Available: www.antinternational.com

[20] P. Atkins and J. De Paula, *Atkins- Physical Chemistry*, 10th ed. London: Oxford University Press, 2014.

[21] T. Rooth, M. Ullberg, E. Karlsson, and I. Persson, “Hydrogen Peroxide in BWRs: An Experimental Determination of The Actual Level,” in *Conference of Water Chemistry of Nuclear Reactor Systems, Vol. 2*, Bournemouth, UK, 1989, pp. 55–60.

[22] C. D. Bopp and O. Sisman, “RADIATION STABILITY OF PLASTICS AND ELASTOMERS (SUPPLEMENT TO ORNL-928),” Jul. 1953, doi: 10.2172/4412528.

[23] A. Charlesby, “Effect of High-energy Radiation on Long-chain Polymers,” *Nature 1953 171:4343*, vol. 171, no. 4343, pp. 167–167, 1953, doi: 10.1038/171167a0.

[24] A. A. Miller, “EFFECTS OF HIGH-ENERGY RADIATION ON POLYMERS,” *Ann N Y Acad Sci*, vol. 82, no. 3, pp. 774–781, 1959, doi: 10.1111/J.1749-6632.1959.TB44957.X.

[25] A. J. . Swallow, *Radiation chemistry of organic compounds*. Pergamon Press, 1960. Accessed: Mar. 24, 2025. [Online]. Available: http://www.sciencedirect.com:5070/book/9780080092973/radiation-chemistry-of-organic-compounds

[26] V. D. Parker, “Chapter 3 Linear Sweep and Cyclic Voltammetry,” *Comprehensive Chemical Kinetics*, vol. 26, no. C, pp. 145–202, Jan. 1986, doi: 10.1016/S0069-8040(08)70027-X.

[27] Pine Research, “Electrochemical Impedance Spectroscopy (EIS) Basics.” Accessed: Apr. 08, 2025. [Online]. Available: https://pineresearch.com/support-article/eis-basics/

[28] A. Visibile, L. Gagliani, E. Ahlberg, J.-E. Svensson, and J. Froitzheim, “An Alternative Method of Measuring Area Specific Resistance of Chromia Scales Using

Electrochemical Impedance Spectroscopy," *J Electrochem Soc*, vol. 170, no. 3, p. 031505, Mar. 2023, doi: 10.1149/1945-7111/acc13e.

[29] P. H. Fang and W. S. Brower, "Dielectric Constant of Cr2O3 Crystals," *Physical Review*, vol. 129, no. 4, p. 1561, Feb. 1963, doi: 10.1103/PhysRev.129.1561.

[30] J. Liu, J. Li, J. Wu, and J. Sun, "Structure and Dielectric Property of High-k ZrO2 Films Grown by Atomic Layer Deposition Using Tetrakis(Dimethylamido)Zirconium and Ozone," *Nanoscale Res Lett*, vol. 14, no. 1, pp. 1–12, May 2019, doi: 10.1186/S11671-019-2989-8/FIGURES/11.

[31] GW Ceramics, "Electrical properties of zirconia, table." Accessed: Apr. 08, 2025. [Online]. Available: https://gwceramics.com/materials/zirconia/

[32] FrancoCorradi SAS, "Proprietà Termo-Fisiche dei componenti di Zirconia, Table." Accessed: Apr. 08, 2025. [Online]. Available: https://francocorradi.it/metalli-e-ceramiche/ceramiche-tecniche/componenti-di-zirconia/

[33] K. V. Rao and A. Smakula, "Dielectric Properties of Cobalt Oxide, Nickel Oxide, and Their Mixed Crystals," *J Appl Phys*, vol. 36, no. 6, pp. 2031–2038, Jun. 1965, doi: 10.1063/1.1714397.

[34] "Ultraviolet absorption spectra of iodine, iodide ion and triiodide ion." Accessed: Apr. 23, 2025. [Online]. Available: https://www.researchgate.net/publication/7884754_Ultraviolet_absorption_spectra_of_iodine_iodide_ion_and_triiodide_ion

[35] N. L. Hansson, "Oxidative dissolution of UO2 by α-radiolysis," 2022, Accessed: Apr. 23, 2025. [Online]. Available: https://research.chalmers.se/en/publication/531458

[36] S. Hanawa *et al.*, "Determination of electrochemical corrosion potential along the JMTR in-pile loop-II: Validation of ECP electrodes and the extrapolation of measured ECP data," *Nucl Technol*, vol. 183, no. 1, pp. 136–148, 2013, doi: 10.13182/NT13-A16998.

[37] M. C. Biesinger, B. P. Payne, L. W. M. Lau, A. Gerson, and R. S. C. Smart, "X-ray photoelectron spectroscopic chemical state quantification of mixed nickel metal, oxide and hydroxide systems," *Surface and Interface Analysis*, vol. 41, no. 4, pp. 324–332, Apr. 2009, doi: 10.1002/SIA.3026.

[38] M. C. Biesinger, B. P. Payne, A. P. Grosvenor, L. W. M. Lau, A. R. Gerson, and R. S. C. Smart, "Resolving surface chemical states in XPS analysis of first row transition metals, oxides and hydroxides: Cr, Mn, Fe, Co and Ni," *Appl Surf Sci*, vol. 257, no. 7, pp. 2717–2730, Jan. 2011, doi: 10.1016/J.APSUSC.2010.10.051.

[39] C. Morant, J. M. Sanz, L. Galán, L. Soriano, and F. Rueda, "An XPS study of the interaction of oxygen with zirconium," *Surf Sci*, vol. 218, no. 2–3, pp. 331–345, Aug. 1989, doi: 10.1016/0039-6028(89)90156-8.

Appendix A – Scale Thickness Determination Techniques

Scanning Electron Microscopy

The surface of the samples was investigated with a Scanning Electron Microscope (SEM) at the Chalmers Materials Analysis Laboratory (CMAL). The investigations were performed with a FEI Quanta ESEM, using both backscattered and secondary electrons detectors. Energy Dispersive X-ray analysis was also performed to ascertain the homogeneity of samples' composition.

X-ray Photoelectron Spectroscopy

XPS analysis of the samples was performed at the Royal Technological University, KTH in Stockholm, by a fellow PhD candidate, Fredrik Petersson. The instrument used was a Kratos Axis Supra+, equipped with a monochromatic Al K(alpha) X-ray source at 1.486.6 eV. The investigated spot area was 700 x 300 µm. X-ray Power was set at 5 mA, 15 kV, 75 W for the collection of wide spectra and 15 mA, 15 kV, 225 W for high-resolution core-level spectra. Charge neutralisation was used with the electron flood gun within the spectrometer. All spectra have been charge corrected to the main line of carbon 1s, which was referenced to 284.8 eV. Backgrounds were fit using the Shirley background. Metallic peaks were fit using asymmetric peak shapes, oxides/hydroxides were fit using 70% Gaussian, 30% Lorentzian peak shapes. Peak fitting was based on the instrument database and the following publications for Ni[37], Fe, Ni and Cr[38], and Zr[39].

Appendix B – Solubilised element investigation

Inductively Coupled Plasma Mass Spectroscopy

For the identification of ions in solution, concentrations were determined using an Inductively Coupled Plasma Mass Spectroscopy (ICP-MS) setup (Thermo Scientific, iCAP Q). The sample solutions were diluted in a 1:2 ratio with 0.5 M HNO_3 (Suprapur, Merck) containing 2ppb of Sc-45 and Y-89 as internal standards (diluted from 10 ppm certified standard solutions, CPAchem). All the measurements were performed in triplicate, in standard mode.